

Tracking Local pH Dynamics During Water Electrolysis via In-line Continuous Flow Raman Spectroscopy

Raul A. Marquez,¹ Jay T. Bender,² Shashwati C. da Cunha,² Ashton M. Aleman,^{3,4} Amareesh Sahu,² Venkat Ganesan,² Delia J. Milliron,^{1,2,6,7} Joaquin Resasco,^{2,7} Thomas F. Jaramillo,^{3,4} and C. Buddie Mullins^{1,2,5,6,7,*}

¹ Department of Chemistry, The University of Texas at Austin, Austin, TX 78712, USA.

² McKetta Department of Chemical Engineering, The University of Texas at Austin, Austin, TX 78712, USA.

³ Department of Chemical Engineering, Stanford University, Stanford, CA 94305, USA.

⁴ SUNCAT Center for Interface Science and Catalysis, SLAC National Accelerator Laboratory, Menlo Park, CA 94025, USA

⁵ Texas Materials Institute, The University of Texas at Austin, Austin, Texas 78712, United States.

⁶ Allen J. Bard Center for Electrochemistry, The University of Texas at Austin, Austin, Texas 78712, United States.

⁷ H2@UT, The University of Texas at Austin, Austin, Texas 78712, United States.

* Corresponding author: mullins@che.utexas.edu

Number of pages: 63

Number of figures and schemes: 26

Number of tables: 12

Table of Contents

S1. Materials and reagents	3
S2. Electrochemical flow cell setup	5
S3. Mass transfer characterization of the electrochemical flow cell	7
S4. In-line continuous flow Raman spectroscopy measurements	11
S5. Analytical modeling of interfacial pH swings – Nocera pH model	13
S6. Analytical modeling of interfacial pH swings – COMSOL model	19
Supporting figures, tables, and schemes.....	29
Mass transfer characterization of the electrochemical flow cell	29
In-line CFRS experiments using PMP electrolyte under alkaline conditions	31
In-line CFRS experiments using PMP electrolyte under near-neutral conditions	35
Analytical modeling of interfacial pH swings	38
In-line CFRS method validation and applicability.....	45
References	61

S1. Materials and reagents

All the electrolytes were prepared using CO₂-free deionized (DI) water (18.2 MΩ·cm). To remove CO₂, DI water was boiled in a 1 L borosilicate Florence flat-bottom flask, cooled to room temperature in the sealed flask, and stored in polypropylene bottles wrapped with Parafilm. Phosphate buffers were used as molecular probes, following previous studies.^{1,2} However, based on critical considerations for using phosphate-buffered saline (PBS) electrolytes in water-splitting studies,³ no additional salts or components (e.g., NaCl) were added. To ensure clarity in the literature, we designated these electrolytes as phosphate molecular probe (PMP) electrolytes.

PMP electrolytes were prepared at a concentration of 0.5 mol·L⁻¹ using reagent-grade potassium phosphate (PO₄³⁻), potassium hydrogen phosphate (HPO₄²⁻), and potassium dihydrogen phosphate (H₂PO₄⁻) (Sigma Aldrich, 99.9%, per certificate of analysis). The component ratios were based on the target pK_a of the phosphoric acid equilibrium: pK_{a,2} = 7.20 (HPO₄²⁻/H₂PO₄⁻) for near-neutral and pK_{a,3} = 12.36 (PO₄³⁻/HPO₄²⁻) for alkaline PMP electrolytes. For calibration curves, the pH was adjusted using 6 M nitric acid (VWR Chemicals BDH, ARISTAR PLUS, 67–70%) or 6 M potassium hydroxide (Sigma Aldrich, 89.5%, per certificate of analysis).

Platinum foil (Thermo Fisher Scientific, Premion™ 99.99% metals basis, thickness: 0.1 mm) was used as the working and counter electrodes in all CFRS measurements. Prior to experiments, Pt foil electrodes (10 × 45 mm) were cleaned in ethanol (Pharmco, 99.5%) via sonication for 10 minutes, followed by electropolishing in a polytetrafluoroethylene (PTFE)

cell. Electropolishing was performed at 500 mA for 60 seconds per side of the foil in ~15 mL of 50 wt% sulfuric acid (Supelco, ACS grade, 96.6%), using the Pt foil as the positive electrode and Pt gauze (Thermo Fisher Scientific, 99.9% metals basis, 52 mesh woven from 0.1 mm wire) as the negative electrode (interelectrode gap: 10 mm). After electropolishing, the Pt foils were rinsed with DI water and assembled into the flow cell.

S2. Electrochemical flow cell setup

The electrochemical flow cell setup consists of a rectangular cell body with a threaded cap at the top, providing a clear visualization of the flow channel. Photos of the assembled cell are shown in **Figure S1**. The cell body and cap were made of acrylic and fabricated using computer numerical control (CNC) machining. PFA film (Chemours, thickness: 0.001 in) was used as a transparent window, enabling the laser to access the electrolyte within the flow channel. A 15 × 15 mm sheet of PFA film was placed on top of the flow channel and secured using a PTFE fixer and a gasket held in place by the threaded cap.

The rectangular flow channel inside the cell measures 10 × 15 × 5 mm, with a total volume of 0.75 mL. Electrodes are positioned on opposite faces of the channel, with the working and counter electrodes facing each other (see **Figure S1b**). The exposed geometric area of each electrode is 0.5 cm², and all current densities in this study are normalized to this area. Polydimethylsiloxane (PDMS) gaskets were used to ensure a tight seal during assembly. 3D models of this electrochemical flow cell are freely available on this [GitHub Repository](#).

Once assembled, the flow cell was integrated into the flow system. A 250 mL Class A glass media bottle served as the electrolyte reservoir, with the cap modified to include two hose barbed fittings (3/16 inch) as tubing connectors. High-temperature silicone tubing (Fuel Cell Store, 4 mm ID × 6 mm OD) was selected for its durability in the flow circuit. The electrolyte was circulated using peristaltic pumps (KAMOER) equipped with Norprene chemical tubing (3.2 mm ID × 6.4 mm OD), with adjustable flow rates between 50 and 200

$\text{mL}\cdot\text{min}^{-1}$. Flow rates for both catholyte and anolyte streams were monitored using a liquid flow controller connected to Hall sensor-equipped flow meters (DIGITEN, Model DFC15). Silicone tubing was carefully connected to the barbed fittings of the flow cell (see **Figures 1a** and **b** in the Main Text).

Fresh PMP electrolytes were used for each test. Before measurements, electrolytes were degassed with high-purity N_2 for 30 minutes using a plastic bubbler. The electrolytes were circulated through the system and into the flow cell to eliminate trapped air within the rectangular channel, ensuring steady flow rates. Electrochemical experiments were conducted in a two-electrode configuration, where the counter electrode (CE) and reference electrode (RE) alligator clips were connected to the counter electrode, while the working electrode (WE) alligator clip was attached to the electrode under study (see **Figure 1a**).

This cell design was specifically developed for use with metal foil electrodes. However, researchers are encouraged to modify the design to accommodate other electrode geometries. Nanoparticulate catalysts could be deposited on flexible substrates (e.g., carbon felts or metallic foams) or applied as thin films on metal foils, bent to fit the cell assembly. Note that complex morphologies and 3D electrodes may introduce additional challenges. For example, highly rough surfaces can create uneven boundaries between the electrode and electrolyte, affecting measurement accuracy. Ideally, the electrode surface should be as flat and smooth as possible. Additionally, electrodes with gaps and pores may form voids where ions or bubbles become trapped, complicating local pH measurements.

S3. Mass transfer characterization of the electrochemical flow cell

The mass transfer properties of the electrochemical flow cell were characterized following established guidelines.^{4,5} Mass transfer coefficients were determined by limiting current measurements of ferricyanide ion reduction on nickel electrodes, with sodium carbonate as the background electrolyte. Nickel foil electrodes (Thermo Fisher Scientific, 99.5% metals basis, thickness: 0.1 mm) were electropolished using the same procedure as platinum foil, with nickel foam as the counter electrode. After polishing, the electrodes were rinsed with DI and assembled into the flow cell. Fresh electrolytes were prepared with analytical-grade reagents (purity ≥99%, Sigma-Aldrich), then degassed with ultra-high-purity argon gas for 30 minutes before each experiment. The composition and other relevant properties of the electrolyte are summarized in **Table S1**.

As shown in **Figures S1c** and **d**, an Ag/AgCl reference electrode was used exclusively for mass transfer characterization. This electrode was positioned upstream in the flow circuit using a tee fitting. The electrolyte reservoir was filled with ~200 mL and circulated at a fixed flow rate. Limiting current measurements of ferricyanide ion reduction were performed to characterize the mass transfer regime. In this method, the limiting current density (j_L) increases proportionally with the flow rate when the system operates under complete mass transfer control (**Figure S2a**). For ferricyanide reduction, this regime is achieved at -0.4 V vs. Ag/AgCl. Once this potential was identified, steady-state measurements were conducted by polarizing the electrode at -0.4 V vs. Ag/AgCl for 120 seconds at varying flow rates (**Figure S2b**). The steady-state current measured during these chronoamperometry runs corresponds to j_L .

Table S1. Flow cell and electrolyte properties for mass transfer characterization.

Interelectrode gap, S	10 mm
Flow channel width, B	10 mm
Flow channel length, L	15 mm
Flow channel height, H	5 mm
Projected geometrical electrode area, $A_{geo} = HL$	0.5 cm ²
Equivalent diameter of the channel, $d_e = 2BH/(B + H)$	6.67 mm
Cross section area of the channel, $A_{cross} = HB$	0.5 cm ²
Dimensionless length, $L_e = d_e/L$	0.444
Electrode compartment volume, V_e	0.75 cm ³
Volumetric flow rate, Q (50 – 200 mL·min ⁻¹)	0.83 – 3.33 cm ³ ·s ⁻¹
Reynolds number, Re (50 – 200 mL·min ⁻¹)	116 – 465
Mean linear flow velocity, v = Q/A _{cross}	1.67 – 6.67 cm·s ⁻¹
Electrolyte composition	1 mM K ₃ Fe(CN) ₆ 10 mM K ₄ Fe(CN) ₆ 1 M Na ₂ CO ₃
Electrolyte density, ρ	1098.5 kg·m ⁻³
Electrolyte kinematic viscosity, ν	9.56 × 10 ⁻³ cm ² ·s ⁻¹
Schmidt number, Sc	1494
Temperature	298.15 ± 0.5 K
Diffusion coefficient of ferricyanide ion, D	6.4 × 10 ⁻⁶ cm ² ·s ⁻¹

The product of the mass transfer coefficient and active electrode area, $k_m A$, was calculated from the limiting current values using **Eq. S1:**⁶

$$k_m A = \frac{j_L}{nF c_b} \quad (\text{S1})$$

where n is the number of electrons transferred, F is Faraday's constant, and c_b is the bulk concentration of electroactive species. The mass transfer to a planar electrode was then estimated using the following empirical correlation:^{6,7}

$$Sh = aRe^b Sc^{0.33} L_e^{0.33} \quad (\text{S2})$$

where Re , Sh , Sc , and L_e are the Reynolds number, Sherwood number, Schmidt number, and dimensionless length, respectively, defined as follows:^{6,8}

$$Re = \frac{ud_e}{\nu} \quad (\text{S3})$$

$$Sc = \frac{\nu}{D} \quad (\text{S4})$$

$$Sh = \frac{k_m d_e}{D} \quad (\text{S5})$$

$$L_e = \frac{d_e}{L} \quad (\text{S6})$$

In these equations, u is the mean linear velocity of the fluid, $d_e = 2BH/(B + H)$ is the equivalent diameter, H is the flow channel height, B is the channel width, ν is the kinematic viscosity of the electrolyte, D is the diffusion coefficient of ferricyanide, and L is the flow channel length.

The apparent diffusion boundary layer thickness (δ) was estimated from the mass transfer coefficient using:⁹

$$\delta = \frac{D}{k_m} \quad (S7)$$

Figure S2c shows a plot of $k_m A$ as a function of the mean linear flow velocity. At approximately 3 cm·s⁻¹ (corresponding to ~90 mL·min⁻¹), a linear increase of $k_m A$ is observed with the flow rate. Similarly, as shown in **Figure S2d**, the linear relationship between the Sherwood (Sh) and Reynolds (Re) numbers establishes the validity of **Eq. S2**, with fitting constants displayed as insets in **Figure S2d**. These mass transfer parameters are useful for scaling studies or comparing hydrodynamics across systems with different cell architectures. Likely, the flow was not fully developed due to the absence of a calming section between the inlet and the electrode surface.⁷ This also explains the steeper slope (b value) in **Figure S2d**.

Finally, **Figure S2e** shows the apparent diffusion boundary layer thickness as a function of the mean linear flow velocity and flow rate. As expected, δ decreases with increasing flow rate, from ~40 µm at 50 mL·min⁻¹ ($Re = 116$) to ~15 µm at 200 mL·min⁻¹ ($Re = 465$). For this study, we focused on two flow rates: 50 mL·min⁻¹ ($\delta = 40$ µm, $Re = 116$) and 100 mL·min⁻¹ ($\delta = 30$ µm, $Re = 233$). The decision to exclude 200 mL·min⁻¹ was due to pronounced periodic fluctuations caused by the peristaltic pump at higher flow rates and the minimal difference in δ between shorter intervals.

S4. In-line continuous flow Raman spectroscopy measurements

Electrochemical measurements

Electrochemical measurements were performed using a Gamry Reference 620 potentiostat/galvanostat. The open circuit potential (OCP) was recorded for 30 minutes to allow the cell to equilibrate. Once a stable OCP was achieved and the flow rate was set, a constant current step was applied via chronopotentiometry for 300 seconds. Raman spectroscopy measurements were conducted 120 seconds after initiating the constant current step, corresponding to the stabilization of the cell potential. Anodic and cathodic current densities of 0 (OCP only), 50, 100, and 200 mA·cm⁻². A constant flow rate was maintained to ensure effective bubble removal from the electrode surface.

Raman spectroscopy measurements

Raman measurements were conducted using a Horiba LabRAM ARAMIS confocal Raman microscope equipped with a 50× magnification objective (Olympus LMPLFLN). A green 532 nm laser was chosen to produce a higher spatial resolution,¹⁰ and operated at 50% of its total power. Based on the numerical aperture of the objective (NA = 0.5), the laser spot size was estimated to be ~1.3 μm. Prior to measurements, calibration was verified using a silicon wafer with a peak at 520.7 cm⁻¹.

Considering the specific geometry of the CFRS flow cell, the laser beam was first focused on the PFA window, then moved ~5 μm into the electrolyte in the Z direction. Subsequently, the laser was positioned at a specific XY coordinate relative to the electrode surface. Spectra were recorded with a resolution of 1 cm⁻¹, centered at 900 cm⁻¹ (range: 50

– 1750 cm⁻¹). Each spectrum was collected over 180 seconds, averaging three scans (i.e., accumulations) of 60 seconds (i.e., acquisition time) each. No additional data processing was performed apart from normalizing peak intensities to the maximum values at the extremes of the calibration curve. Importantly, sulfate salts were excluded from the PMP electrolyte to avoid interference with phosphate features, as these salts exhibit overlapping Raman bands.¹⁰ Quantitative analyses were limited to spectra obtained on the same working electrode within the experimental sequence to ensure consistency.

S5. Analytical modeling of interfacial pH swings – Nocera pH model

Veroneau and coworkers published a succinct pH model to obtain the local pH during the oxygen evolution reaction (OER) in buffered solutions.¹¹ Considering the presence of hydroxide ions in solution, the authors obtained the following expression of the proton concentration at the electrode surface, $(C_{H^+})_{x=0}$:

$$(C_{H^+})_{x=0} = \frac{1}{2} \left[\frac{D_B}{D_{H^+}} C_B^0 - \left(\frac{j_{OER}\delta}{FD_{H^+}} + C_{H^+}^0 - K_a \right) \right] + \frac{1}{2} \sqrt{\left[\frac{D_B}{D_{H^+}} C_B^0 - \left(\frac{j_{OER}\delta}{FD_{H^+}} + C_{H^+}^0 - K_a \right) \right]^2 + 4K_a \left(\frac{j_{OER}\delta}{FD_{H^+}} + C_{H^+}^0 + \frac{D_B}{D_{H^+}} C_{BH}^0 \right)} \quad (S8)$$

where D_B is the diffusion coefficient of the deprotonated buffer (B), D_{H^+} is the diffusion coefficient of H^+ , C_B^0 is the bulk concentration of the deprotonated buffer, j is the applied current density, $C_{H^+}^0$ is the bulk concentration of H^+ , K_a is the acid-base equilibrium constant for the buffer species, and C_{BH}^0 is the bulk concentration of the protonated buffer (BH). The step-by-step procedure to derive this expression can be found elsewhere.¹¹

Following the same assumptions, we derived an analogous expression for the hydrogen evolution reaction (HER). First, three electrochemical reactions are considered:

- (1) Water reduction with an acidic component of the buffer (BH^+) as the source of H^+ :



- (2) Water reduction with water as the base:



- (3) Proton reduction



At the electrode surface, $x = 0$, assuming fast proton transfer and, therefore, unconditional equilibrium:

$$K_a = \frac{(C_{\text{H}^+})_{x=0} \cdot (C_{\text{B}})_{x=0}}{(C_{\text{BH}^+})_{x=0}} \quad (\text{S12})$$

$$K_e = (C_{\text{H}^+})_{x=0} \cdot (C_{\text{OH}^-})_{x=0} \quad (\text{S13})$$

At the diffusion layer and bulk solution interface, $x = \delta$:

$$\begin{aligned} (C_{\text{H}^+})_{x=\delta} &= C_{\text{H}^+}^0 \\ (C_{\text{OH}^-})_{x=\delta} &= C_{\text{OH}^-}^0 \\ (C_{\text{B}})_{x=\delta} &= C_{\text{B}}^0 \\ (C_{\text{BH}^+})_{x=\delta} &= C_{\text{BH}^+}^0 \end{aligned} \quad (\text{S14})$$

$$K_a = \frac{C_{\text{H}^+}^0 \cdot C_{\text{B}}^0}{C_{\text{BH}^+}^0} \quad (\text{S15})$$

$$K_e = C_{\text{H}^+}^0 \cdot C_{\text{OH}^-}^0 \quad (\text{S16})$$

In solution,

$$\frac{d^2(C_{\text{B}} + C_{\text{BH}^+})}{dx^2} = 0 \quad (\text{S17})$$

Hence,

$$\frac{d(C_{\text{B}} + C_{\text{BH}^+})}{dx} = \left[\frac{d(C_{\text{B}} + C_{\text{BH}^+})}{dx} \right]_{x=0} = 0 \quad (\text{S18})$$

It follows that,

$$(C_{\text{B}})_{x=0} + (C_{\text{BH}^+})_{x=0} = (C_{\text{B}})_{x=\delta} + (C_{\text{BH}^+})_{x=\delta} = C_{\text{B}}^0 + C_{\text{BH}^+}^0 \quad (\text{S19})$$

In the boundary layer, $0 < x < \delta$:

$$-D_{H^+} \frac{d^2 C_{H^+}}{dx^2} - D_{BH^+} \frac{d^2 C_{BH^+}}{dx^2} + D_{OH^-} \frac{d^2 C_{OH^-}}{dx^2} = 0 \quad (S20)$$

Therefore, the rate for HER is defined as follows:

$$-\frac{j_{HER}}{F} = -D_{H^+} \left(\frac{dC_{H^+}}{dx} \right)_{x=0} - D_{BH^+} \left(\frac{dC_{BH^+}}{dx} \right)_{x=0} + D_{OH^-} \left(\frac{dC_{OH^-}}{dx} \right)_{x=0} \quad (S21)$$

And we also have,

$$D_{BH^+} \left(\frac{dC_{BH^+}}{dx} \right)_{x=0} = -D_B \left(\frac{dC_B}{dx} \right)_{x=0} \quad (S22)$$

Thus,

$$-\frac{j_{HER}}{F} = \frac{(-D_{H^+}C_{H^+} - D_{BH^+}C_{BH^+} + D_{OH^-}C_{OH^-})_{x=\delta} - (-D_{H^+}C_{H^+} - D_{BH^+}C_{BH^+} + D_{OH^-}C_{OH^-})_{x=0}}{\delta} \quad (S23)$$

Leading to,

$$\left(C_{H^+} + \frac{D_{BH^+}}{D_{H^+}} C_{BH^+} - \frac{D_{OH^-}}{D_{H^+}} C_{OH^-} \right)_{x=0} = -\frac{j_{HER}\delta}{FD_{H^+}} + \left(C_{H^+} + \frac{D_{BH^+}}{D_{H^+}} C_{BH^+} - \frac{D_{OH^-}}{D_{H^+}} C_{OH^-} \right)_{x=\delta} \quad (S24)$$

It follows that,

$$(C_{H^+})_{x=0} + \frac{D_{BH^+}}{D_{H^+}} (C_{BH^+})_{x=0} - \frac{D_{OH^-}}{D_{H^+}} (C_{OH^-})_{x=0} = -\frac{j_{HER}\delta}{FD_{H^+}} + C_{H^+}^0 + \frac{D_{BH^+}}{D_{H^+}} C_{BH^+}^0 - \frac{D_{OH^-}}{D_{H^+}} C_{OH^-}^0 \quad (S25)$$

Solving for $(C_{BH^+})_{x=0}$,

$$(C_{BH^+})_{x=0} = -\frac{D_{H^+}}{D_{BH^+}} \cdot \frac{j_{HER}\delta}{FD_{H^+}} + \frac{D_{H^+}}{D_{BH^+}} \left(C_{H^+}^0 - \frac{D_{OH^-}}{D_{H^+}} C_{OH^-}^0 \right) - \frac{D_{H^+}}{D_{BH^+}} \left[(C_{H^+})_{x=0} - \frac{D_{OH^-}}{D_{H^+}} (C_{OH^-})_{x=0} \right] + C_{BH^+}^0 \quad (S26)$$

And using **Eq. S19**, it follows that,

$$(C_B)_{x=0} = C_B^0 + \frac{D_{H^+}}{D_{BH^+}} \cdot \frac{j_{HER}\delta}{FD_{H^+}} - \frac{D_{H^+}}{D_{BH^+}} \left(C_{H^+}^0 - \frac{D_{OH^-}}{D_{H^+}} C_{OH^-}^0 \right) + \frac{D_{H^+}}{D_{BH^+}} \left[(C_{H^+})_{x=0} - \frac{D_{OH^-}}{D_{H^+}} (C_{OH^-})_{x=0} \right] \quad (S27)$$

By substituting **Eqs. S26** and **S27** in **Eq. S12**, it follows that,

$$K_a = \frac{(C_{H^+})_{x=0} \cdot \left\{ C_B^0 + \frac{D_{H^+}}{D_{BH^+}} \cdot \frac{j_{HER}\delta}{FD_{H^+}} - \frac{D_{H^+}}{D_{BH^+}} \left(C_{H^+}^0 - \frac{D_{OH^-}}{D_{H^+}} C_{OH^-}^0 \right) + \frac{D_{H^+}}{D_{BH^+}} \left[(C_{H^+})_{x=0} - \frac{D_{OH^-}}{D_{H^+}} (C_{OH^-})_{x=0} \right] \right\}}{C_{BH^+}^0 - \frac{D_{H^+}}{D_{BH^+}} \cdot \frac{j_{HER}\delta}{FD_{H^+}} + \frac{D_{H^+}}{D_{BH^+}} \left(C_{H^+}^0 - \frac{D_{OH^-}}{D_{H^+}} C_{OH^-}^0 \right) - \frac{D_{H^+}}{D_{BH^+}} \left[(C_{H^+})_{x=0} - \frac{D_{OH^-}}{D_{H^+}} (C_{OH^-})_{x=0} \right]} \quad (S28)$$

And using **Eqs. S13** and **S16** to remove $(C_{OH^-})_{x=0}$ and $C_{OH^-}^0$,

$$K_a = \frac{(C_{H^+})_{x=0} \cdot \left\{ C_B^0 + \frac{D_{H^+}}{D_{BH^+}} \cdot \frac{j_{HER}\delta}{FD_{H^+}} - \frac{D_{H^+}}{D_{BH^+}} \left(C_{H^+}^0 - \frac{D_{OH^-}}{D_{H^+}} \cdot \frac{K_e}{C_{H^+}^0} \right) + \frac{D_{H^+}}{D_{BH^+}} \left[(C_{H^+})_{x=0} - \frac{D_{OH^-}}{D_{H^+}} \cdot \frac{K_e}{(C_{H^+})_{x=0}} \right] \right\}}{C_{BH^+}^0 - \frac{D_{H^+}}{D_{BH^+}} \cdot \frac{j_{HER}\delta}{FD_{H^+}} + \frac{D_{H^+}}{D_{BH^+}} \left(C_{H^+}^0 - \frac{D_{OH^-}}{D_{H^+}} \cdot \frac{K_e}{C_{H^+}^0} \right) - \frac{D_{H^+}}{D_{BH^+}} \left[(C_{H^+})_{x=0} - \frac{D_{OH^-}}{D_{H^+}} \cdot \frac{K_e}{(C_{H^+})_{x=0}} \right]} \quad (S29)$$

Eq. S29 can be simplified if the following conditions are considered:

$$(C_{H^+})_{x=0} \text{ and } C_{H^+}^0 \ll \sqrt{\frac{D_{OH^-}}{D_{H^+}} \cdot K_e} \quad (S30)$$

And,

$$C_{BH^+}^0 \ll \frac{D_{OH^-}}{D_{BH^+}} \cdot C_{OH^-}^0 \quad (S31)$$

Thus, **Eq. S29** becomes,

$$K_a = \frac{(C_{H^+})_{x=0} \cdot \left[C_B^0 + \frac{D_{H^+}}{D_{BH^+}} \cdot \frac{j_{HER}\delta}{FD_{H^+}} - \frac{D_{H^+}}{D_{BH^+}} C_{H^+}^0 + \frac{D_{H^+}}{D_{BH^+}} (C_{H^+})_{x=0} \right]}{-\frac{D_{H^+}}{D_{BH^+}} \cdot \frac{j_{HER}\delta}{FD_{H^+}} + \frac{D_{H^+}}{D_{BH^+}} C_{H^+}^0 - \frac{D_{H^+}}{D_{BH^+}} (C_{H^+})_{x=0} + C_{BH^+}^0} \quad (S32)$$

It follows that,

$$\begin{aligned} \frac{D_{H^+}}{D_{BH^+}} [(C_{H^+})_{x=0}]^2 + \frac{D_{H^+}}{D_{BH^+}} \left(-C_{H^+}^0 + \frac{j_{HER}\delta}{FD_{H^+}} + \frac{D_{BH^+}}{D_{H^+}} C_B^0 + K_a \right) (C_{H^+})_{x=0} \\ - \frac{D_{H^+}}{D_{BH^+}} \left(\frac{D_{BH^+}}{D_{H^+}} C_{BH^+}^0 + C_{H^+}^0 - \frac{j_{HER}\delta}{FD_{H^+}} \right) \cdot K_a = 0 \end{aligned} \quad (S33)$$

Also,

$$[(C_{H^+})_{x=0}]^2 + \left[\frac{D_{BH^+}}{D_{H^+}} C_B^0 - \left(-\frac{j_{HER}\delta}{FD_{H^+}} + C_{H^+}^0 - K_a \right) \right] (C_{H^+})_{x=0} \\ - K_a \cdot \left(-\frac{j_{HER}\delta}{FD_{H^+}} + C_{H^+}^0 + \frac{D_{BH^+}}{D_{H^+}} C_{BH^+}^0 \right) = 0 \quad (S34)$$

Solving for $(C_{H^+})_{x=0}$,

$$(C_{H^+})_{x=0} = -\frac{1}{2} \left[\frac{D_{BH^+}}{D_{H^+}} C_B^0 - \left(-\frac{j_{HER}\delta}{FD_{H^+}} + C_{H^+}^0 - K_a \right) \right] \\ + \frac{1}{2} \sqrt{\left[\frac{D_{BH^+}}{D_{H^+}} C_B^0 - \left(-\frac{j_{HER}\delta}{FD_{H^+}} + C_{H^+}^0 - K_a \right) \right]^2 + 4K_a \left(-\frac{j_{HER}\delta}{FD_{H^+}} + C_{H^+}^0 + \frac{D_{BH^+}}{D_{H^+}} C_{BH^+}^0 \right)} \quad (S35)$$

Eq. S35 gives the surface concentration of H^+ under HER current densities in the presence of a buffer (B/BH^+) and slightly alkaline conditions. This equation is analogous to the OER expression proposed by the Nocera Group (**Eq. S8**).

Table S2 contains the constants and parameters used to construct interfacial pH profiles as a function of the current density. Acid dissociation constants were retrieved from elsewhere (shown in **Table S2** as pK_a values).¹² Diffusion coefficients were retrieved from COMSOL's thermodynamic database. The total bulk concentration of the buffer species was set to $0.5 \text{ mol}\cdot\text{L}^{-1}$. The bulk concentration of protons was estimated from the solution pH (in this case, equal to the studied pK_a) using **Eq. S36**:

$$C_{H^+}^0 = 10^{-pH} \quad (S36)$$

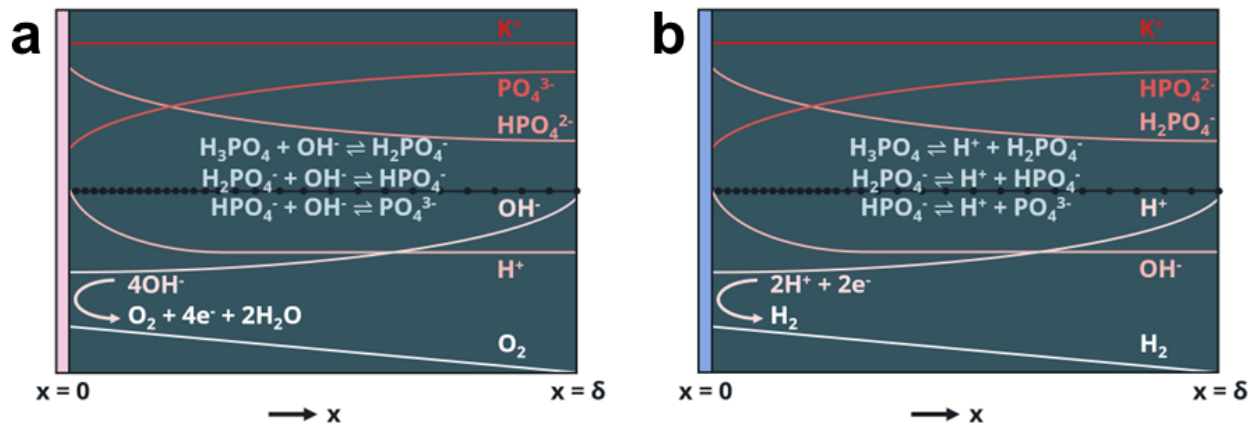
Table S2. Parameters used to construct pH profiles using the Nocera Group's pH model.

Phosphoric acid, $pK_{a,2}$ ($\text{H}_2\text{PO}_4^-/\text{HPO}_4^{2-}$)	7.20
Phosphoric acid, $pK_{a,3}$ ($\text{HPO}_4^{2-}/\text{PO}_4^{3-}$)	12.36
Diffusion coefficient of H^+ , D_{H^+}	$9.31 \times 10^{-5} \text{ cm}^2 \cdot \text{s}^{-1}$
Diffusion coefficient of H_2PO_4^- , D_{BH^+}	$9.59 \times 10^{-6} \text{ cm}^2 \cdot \text{s}^{-1}$
Diffusion coefficient of HPO_4^{2-} , D_{BH^+} (for $pK_{a,3}$), D_{B} (for $pK_{a,2}$)	$7.59 \times 10^{-6} \text{ cm}^2 \cdot \text{s}^{-1}$
Diffusion coefficient of PO_4^{3-} , D_{B}	$8.24 \times 10^{-6} \text{ cm}^2 \cdot \text{s}^{-1}$
Faraday constant, F	96 485.33 C·mol ⁻¹

S6. Analytical modeling of interfacial pH swings – COMSOL model

Galvanostatic model

To model the trends in measured pH, we solve species mass balances using a diffusion-reaction model in the two experimentally tested electrolytes.^{13,14} In Case 1 (alkaline pH), the HER and OER occur in 0.5 M phosphate molecular probe (PMP) electrolyte near $pK_{a,3}$ (0.25 M K_3PO_4 + 0.25 M K_2HPO_4). In Case 2 (near-neutral pH), both reactions occur in 0.5 M PMP near $pK_{a,2}$ (0.25 M K_2HPO_4 + 0.25 M KH_2PO_4). Electrolytes do not contain additional supporting electrolytes. All simulations were solved in one dimension using COMSOL Multiphysics 6.2 with the Electrochemistry package using the PARDISO solver. The finite elements modeling executed by COMSOL reduces to finite differences, and this system of equations is reproducible in any numerical solver. COMSOL was chosen to simplify the post-processing, setup, and handling of the buffering reactions.



Scheme S1. Schematic of the diffusion-reaction model. (a) OER occurring in Case 1, where the buffer composition leads to an alkaline pH. (b) HER occurring in Case 2, where the buffer composition is nearly neutral. Not all species are pictured; concentration profiles are not to scale.

Governing equations

In the diffusion layer within the electrolyte, we assume that the mass transfer of species to and from the surface governs the concentration profile. In this diffusion layer, phosphate buffer species will react to balance the consumption and generation of H^+ and OH^- by electrochemical surface reactions. We also neglect convection, assuming a stagnant diffusion layer. We therefore use the following 1D steady-state diffusion-reaction model, neglecting migration and convection:

$$J_i = -D_i \nabla c_i \quad (\text{S37})$$

$$\nabla \cdot J_i = R_i \quad (\text{S38})$$

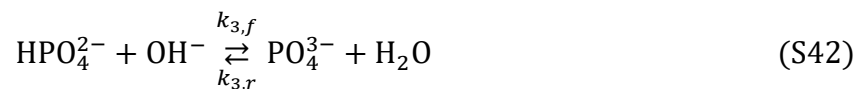
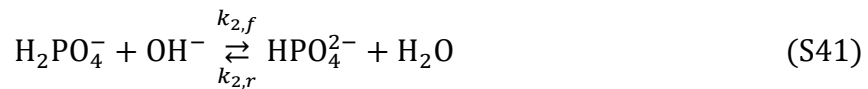
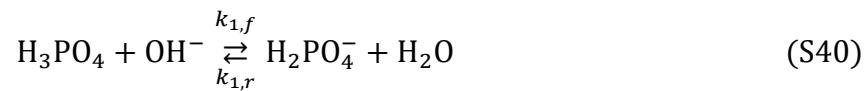
$$D_i \frac{d^2 c_i}{dx^2} + R_i = 0 \quad (\text{S39})$$

where J_i is the 1D flux of species i , D_i is the diffusion coefficient of species i , c_i is the concentration of species i , and R_i is the homogeneous reaction rate.

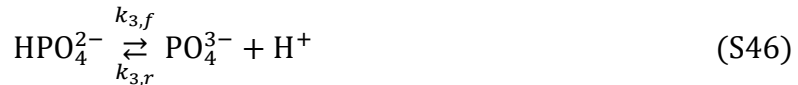
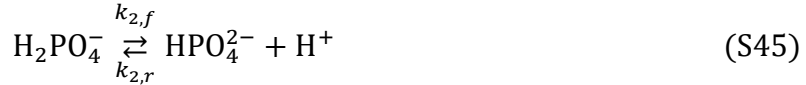
Eq. S37 is Fick's first law. According to Fick's law, mass transport is driven purely by diffusion via concentration gradients. We assume that all species are dilute, allowing the use of literature diffusion coefficients at infinite dilution. Potential, current, and potential-driven migration are not modeled since we found their effect negligible over the length scale of the diffusion layer, where very large concentration gradients are present. Other diffusion-reaction models have also successfully modeled electrochemical phenomena over this length scale.^{11,13,14} **Eq. S39** is the overall mass balance, which specifies that the flux balances the homogeneous reactions.

No momentum transport is modeled, although the experimental setup involves convective flow against the electrode plate. This assumption prevents the introduction of extra assumptions and 2D geometric features, which would be necessary to model a hydrodynamic boundary layer of fluid flow over the electrode. Therefore, we do not model a true boundary layer. Instead, the experimentally measured boundary layer thickness is used as the apparent boundary distance, δ . We, therefore, use the notations bulk and $x=\delta$ interchangeably here. The Péclet number over the diffusion layer of $\delta = 30\mu\text{m}$, assuming $< 99\%$ of the average linear velocity at $100 \text{ mL}\cdot\text{min}^{-1}$ ($0.0256 \text{ m}\cdot\text{s}^{-1}$), is $Pe = u_\delta\delta/D_i < 101.2$, using the slowest diffusing model in the system (HPO_4^{2-} , $D_{\text{HPO}_4^{2-}} = 7.59 \times 10^{-9} \text{ m}^2\cdot\text{s}^{-1}$). This indicates that such a simplifying assumption does not accurately represent the system. However, a 2D hydrodynamic model is beyond the scope of this project, which seeks only to confirm that the expected buffer dynamics can explain the trends in pH measured experimentally.

Based on these equations, there are eight concentration variables, one each for H_3PO_4 , H_2PO_4^- , HPO_4^{2-} , PO_4^{3-} , OH^- , H^+ , H_2 , and O_2 . For Case 1, which is highly alkaline, we model the following homogeneous reactions:



For Case 2, which is nearly neutral, we model the following homogeneous reactions:



The equilibrium constants were obtained from the literature. The equilibria for **Eqs. S44 – S46** are governed by acid dissociation constants: $\text{p}K_{\text{a},1} = 2.16$, $\text{p}K_{\text{a},2} = 7.20$, and $\text{p}K_{\text{a},3} = 12.36$.¹⁵ Therefore, their equilibrium constants are $K_{\text{a},1} = 6.918 \times 10^{-3}$ M, $K_{\text{a},2} = 6.166 \times 10^{-8}$ M, and $K_{\text{a},3} = 4.786 \times 10^{-13}$ M. The equilibrium constant for water dissociation (**Eqs. S43 and S47**), K_w , is 1.01×10^{-14} M. On the other hand, the equilibria for **Eqs. S40 – S42** are governed by K_b^{-1} , where $K_b = K_a \times K_w$. This gives $K_{b,1}^{-1} = 6.850 \times 10^{11}$ M⁻¹, $K_{b,2}^{-1} = 6.105 \times 10^6$ M⁻¹, and $K_{b,3}^{-1} = 47.38$ M⁻¹.

The forward reaction rates for homogeneous reactions are obtained from the literature and given in **Table S3**. For each of the reactions, the reverse reaction rate is obtained using their equilibrium constants:

$$K = \frac{k_f}{k_r} \quad (\text{S48})$$

$$\Rightarrow k_r = \frac{k_f}{K} \quad (\text{S49})$$

Combining the above reactions with the overall mass balance, **Eq. S39**, we obtain the following governing equations for the eight variables for Case 1 (alkaline pH):

$$\begin{aligned}
D_{H_3PO_4} \frac{d^2 c_{H_3PO_4}}{dx^2} & -k_{1,f} \times c_{H_3PO_4} \times c_{OH^-} + k_{1,r} \times c_{H_2PO_4^-} = 0 \\
D_{H_2PO_4^-} \frac{d^2 c_{H_2PO_4^-}}{dx^2} & -k_2 f \times c_{H_2PO_4^-} \times c_{OH^-} + k_{2,r} \times c_{HPO_4^{2-}} + k_{1f} \times c_{H_3PO_4} \times c_{OH}^- - k_{1,r} \times c_{H_2PO_4^-} = 0 \\
D_{HPO_4^{2-}} \frac{d^2 c_{HPO_4^{2-}}}{dx^2} & -k_{3,f} \times c_{HPO_4^{2-}} \times c_{OH}^- + k_{3,r} \times c_{PO_4^{3-}} + k_{2,f} \times c_{H_2PO_4^-} \times c_{OH}^- - k_{2,r} \times c_{HPO_4^{2-}} = 0 \\
D_{PO_4^{3-}} \frac{d^2 c_{PO_4^{3-}}}{dx^2} & +k_{3,f} \times c_{HPO_4^{2-}} \times c_{OH}^- - k_{3,r} \times c_{PO_4^{3-}} = 0 \\
D_{H^+} \frac{d^2 c_{H^+}}{dx^2} & +k_{w,f} - k_{w,r} \times c_H^+ \times c_{OH}^- = 0 \\
D_{OH^-} \frac{d^2 c_{OH^-}}{dx^2} & -k_{1f} \times c_{H_3PO_4} \times c_{OH}^- + k_{1,r} \times c_{H_2PO_4^-} - k_{2,f} \times c_{H_2PO_4^-} \times c_{OH}^- + k_{2,r} \times c_{HPO_4^{2-}} \\
& -k_{3,f} \times c_{HPO_4^{2-}} \times c_{OH}^- + k_{3,r} \times c_{PO_4^{3-}} + k_{w,f} - k_{w,r} \times c_H^+ \times c_{OH}^- = 0 \\
D_{K^+} \frac{d^2 c_{K^+}}{dx^2} & = 0 \\
D_{H_2} \frac{d^2 c_{H_2}}{dx^2} & = 0 \\
D_{O_2} \frac{d^2 c_{O_2}}{dx^2} & = 0
\end{aligned}$$

Similarly, we obtain the following governing equations for the eight variables for Case 2 (near-neutral pH):

$$\begin{aligned}
D_{H_3PO_4} \frac{d^2 c_{H_3PO_4}}{dx^2} & -k_{1,f} \times c_{H_3PO_4} + k_{1,r} \times c_{H_2PO_4^-} \times c_{H^+} = 0 \\
D_{H_2PO_4^-} \frac{d^2 c_{H_2PO_4^-}}{dx^2} & -k_{2,f} \times c_{H_2PO_4^-} + k_{2,r} \times c_{HPO_4^{2-}} \times c_{H^+} + k_{1,f} \times c_{H_3PO_4} - k_{1,r} \times c_{H_2PO_4^-} \times c_{H^+} = 0 \\
D_{HPO_4^{2-}} \frac{d^2 c_{HPO_4^{2-}}}{dx^2} & -k_{3,f} \times c_{HPO_4^{2-}} + k_{3,r} \times c_{PO_4^{3-}} \times c_{H^+} + k_{2,f} \times c_{H_2PO_4^-} - k_{2,r} \times c_{HPO_4^{2-}} \times c_{H^+} = 0 \\
D_{PO_4^{3-}} \frac{d^2 c_{PO_4^{3-}}}{dx^2} & +k_{3,f} \times c_{HPO_4^{2-}} - k_{3,r} \times c_{PO_4^{3-}} \times c_{H^+} = 0 \\
D_{H^+} \frac{d^2 c_{H^+}}{dx^2} & +k_{3,r} \times k_{w,f} - k_{w,r} \times c_{H^+} \times c_{OH^-} + k_{1,f} \times c_{H_3PO_4} - k_{1,r} \times c_{H_2PO_4^-} \times c_{H^+} \\
& +k_{2,f} \times c_{H_2PO_4^-} - k_{2,r} \times c_{HPO_4^{2-}} \times c_{H^+} + k_{3,f} \times c_{HPO_4^{2-}} - k_{3,r} \times c_{PO_4^{3-}} \times c_{H^+} = 0 \\
D_{OH^-} \frac{d^2 c_{OH^-}}{dx^2} & +k_{3,r} \times k_{w,f} - k_{w,r} \times c_{H^+} \times c_{OH^-} = 0 \\
D_{K^+} \frac{d^2 c_{K^+}}{dx^2} & = 0 \\
D_{H_2} \frac{d^2 c_{H_2}}{dx^2} & = 0 \\
D_{O_2} \frac{d^2 c_{O_2}}{dx^2} & = 0
\end{aligned}$$

Boundary conditions (BCs)

The two 1D boundaries are the electrode surface ($x = 0$) and the bulk electrolyte at its boundary distance ($x = \delta$). At the electrolyte bulk, all concentrations are specified (Dirichlet boundary conditions). At the electrode surface, all fluxes are specified (Neumann boundary conditions). For the second-order differential equation for each species (**Eq. S39**), these two BCs are sufficient to specify the system.

BCs at $x = \delta$

We assume the electrolyte was well-mixed at the bulk due to forced convection (pumping), allowing all the acid-base reactions to equilibrate. The experimental concentration of buffers was used to determine the bulk concentration of H^+ using the Henderson-Hasselbach equation:

$$pH_{bulk, Case\ 1} = pK_{a,3} + \log_{10} \left(\frac{c_{PO_4,bulk}}{c_{HPO_4,bulk}} \right) \quad (S50)$$

$$pH_{bulk, Case\ 2} = pK_{a,2} + \log_{10} \left(\frac{c_{HPO_4,bulk}}{c_{H_2PO_4,bulk}} \right) \quad (S51)$$

$$c_{\text{H}^+}|_{x=\delta} = 10^{-pH_{bulk}} \quad (S52)$$

$$c_{\text{OH}^-}|_{x=\delta} = 10^{-(14-pH_{bulk})} \quad (S53)$$

According to **Eqs. S50** and **S51**, the bulk pH was 12.522 for Case 1 and 8.006 for Case 2. The bulk pH was also calculated via a more detailed model correcting for ionic strength,¹⁶ which gave a theoretical bulk pH of 12.656 for Case 1 and 7.797 for Case 2. The experimentally measured bulk pH via pH meter was 12.52 for Case 1 and 7.63 for Case 2. All three bulk pH values are within experimental error.

Due to mixing, the concentration of products is zero in the bulk:

$$c_{O_2}|_{x=\delta} = 0 \quad (S54)$$

$$c_{H_2}|_{x=\delta} = 0 \quad (S55)$$

The bulk concentration of the phosphate buffer species (H_3PO_4 , $H_2PO_4^-$, HPO_4^{2-} , PO_4^{3-}) and their counterion, K^+ , come from the specified salt concentration. For example, for Case 1 at pH 12.32:

$$c_{H_3PO_4}|_{x=\delta} = 0 \quad (S56)$$

$$c_{H_2PO_4^-}|_{x=\delta} = 0 \quad (S57)$$

$$c_{PO_4^{3-}}|_{x=\delta} = 0.30725 \text{ M} \quad (S58)$$

$$c_{HPO_4^{2-}}|_{x=\delta} = 0.5 \text{ M} - 0.30725 \text{ M} = 0.19275 \text{ M} \quad (S59)$$

$$c_{K^+}|_{x=\delta} = 2 \times c_{HPO_4^{2-}}|_{x=\delta} + 3 \times c_{PO_4^{3-}}|_{x=\delta} \quad (S60)$$

BCs at $x = 0$

Flux is modeled by Fick's first law in this dilute system:

$$J_i = D_i \frac{dc_i}{dx} \quad (S61)$$

By convention, positive flux represents the influx of species from the electrode to the electrolyte, while negative represents the consumption of electrolyte species. At the electrode surface, we assume that the HER and OER lead to surface fluxes for O_2 (for OER), H_2 (for HER), OH^- (for Case 1 near $pK_{a,3}$), and H^+ (for Case 2 near $pK_{a,2}$). There is no flux for other species:

$$J_{H_3PO_4}|_{x=0} = 0 \quad (S62)$$

$$J_{H_2PO_4^-}|_{x=0} = 0 \quad (S63)$$

$$J_{HPO_4^{2-}}|_{x=0} = 0 \quad (S64)$$

$$J_{PO_4^{3-}}|_{x=0} = 0 \quad (S65)$$

$$J_{K^+}|_{x=0} = 0 \quad (S66)$$

O_2 and H_2 surface fluxes are calculated at a given current density using Faraday's law:

$$R_{OER} = \frac{j_{OER}}{4F} \quad (S67)$$

$$R_{HER} = \frac{-j_{HER}}{2F} \quad (S68)$$

$$J_{O_2}|_{x=0} = R_{OER} \quad (S69)$$

$$J_{H_2}|_{x=0} = R_{HER} \quad (S70)$$

where F is Faraday's constant. We assume perfect selectivity towards H_2 at negative and O_2 at positive current densities. Water oxidation to hydrogen peroxide via a 2-electron process is neglected.

For Case 1, OH^- and H^+ fluxes are calculated as follows:

$$J_{OH^-}|_{x=0} = -4R_{OER} + 2R_{HER} \quad (S71)$$

$$J_{H^+}|_{x=0} = 0 \quad (S72)$$

For Case 2, OH^- and H^+ fluxes are calculated as follows:

$$J_{OH^-}|_{x=0} = 0 \quad (S73)$$

$$J_{H^+}|_{x=0} = 4R_{OER} - 2R_{HER} \quad (S74)$$

Geometry

The modeled geometry is one-dimensional from the electrode surface to the bulk electrolyte. The apparent diffusion layer thickness δ was based on experimentally measured values. Experiments gave a boundary layer thickness of 30.5 μm at 100 $mL \cdot min^{-1}$ electrolyte circulation and 40 μm at 50 $mL \cdot min^{-1}$. The 1D finite element length was at most 1 μm from $x = 1 \mu m$ to $x = \delta$ and at most 0.001 μm from $x = 0 \mu m$ to $x = 1 \mu m$. Element length transitioned smoothly in the region of approximately 1 to 2 μm with a maximum growth rate of 1.2. A node was also added at 10 μm to mimic the experimental probe position.

Table S3. Parameters used to construct local pH profiles using the COMSOL model.

Description	Value	Ref.
Bulk concentration of K_2HPO_4 in Case 2	0.25	This work
Bulk concentration of K_3PO_4 in Case 1	0.25	This work
Bulk concentration of total phosphate salts	0.500	This work
Diffusion coefficient of H^+ in water, D_{H^+}	$9.31 \times 10^{-5} \text{ cm}^2\cdot\text{s}^{-1}$	15
Diffusion coefficient of O_2 in water, D_{O_2}	$2.01 \times 10^{-5} \text{ cm}^2\cdot\text{s}^{-1}$	15
Diffusion coefficient of H_2 in water, D_{H_2}	$4.58 \times 10^{-5} \text{ cm}^2\cdot\text{s}^{-1}$	15
Diffusion coefficient of K^+ in water, D_{K^+}	$1.96 \times 10^{-5} \text{ cm}^2\cdot\text{s}^{-1}$	15
Diffusion coefficient of H_3PO_4 , $D_{\text{H}_3\text{PO}_4}$	$8.70 \times 10^{-6} \text{ cm}^2\cdot\text{s}^{-1}$	15
Diffusion coefficient of H_2PO_4^- , $D_{\text{H}_2\text{PO}_4^-}$	$9.59 \times 10^{-6} \text{ cm}^2\cdot\text{s}^{-1}$	15
Diffusion coefficient of HPO_4^{2-} , $D_{\text{HPO}_4^{2-}}$	$7.59 \times 10^{-6} \text{ cm}^2\cdot\text{s}^{-1}$	15
Diffusion coefficient of PO_4^{3-} , $D_{\text{PO}_4^{3-}}$	$8.24 \times 10^{-6} \text{ cm}^2\cdot\text{s}^{-1}$	15
Diffusion coefficient of OH^- in water, D_{OH^-}	$5.27 \times 10^{-5} \text{ cm}^2\cdot\text{s}^{-1}$	15
Apparent diffusion layer thickness, δ , at $100 \text{ mL}\cdot\text{min}^{-1}$	$30.5 \mu\text{m}$	This work
Equilibrium constant, water dissociation, K_w	$1.01 \times 10^{-14} \text{ M}$	15
Faraday constant, F	96 485.33 C·mol ⁻¹	9
Forward rate, H_3PO_4 to H_2PO_4^- , acidic, $k_{1,f}$	$5.6 \times 10^8 \text{ s}^{-1}$	17
Forward rate, H_3PO_4 to H_2PO_4^- , alkaline, $k_{1,a}$	$4.2 \times 10^4 \text{ M}^{-1}\cdot\text{s}^{-1}$	18
Forward rate, H_2PO_4^- to HPO_4^{2-} , acidic, $k_{2,f}$	$3.1 \times 10^6 \text{ s}^{-1}$	19
Forward rate, H_2PO_4^- to HPO_4^{2-} , alkaline, $k_{2,a}$	$2.0 \times 10^4 \text{ M}^{-1}\cdot\text{s}^{-1}$	20
Forward rate, HPO_4^{2-} to PO_4^{3-} , acidic, $k_{3,f}$	$1.4 \times 10^5 \text{ s}^{-1}$	19

Forward rate, HPO_4^{2-} to PO_4^{3-} , alkaline, $k_{3,f}$	$1.5 \times 10^5 \text{ M}^{-1}\cdot\text{s}^{-1}$	20
Forward rate of reaction, water dissociation, $k_{w,f}$	$2.4 \times 10^{-5} \text{ M}\cdot\text{s}^{-1}$	21,22
First dissociation, $\text{p}K_{a,1} (\text{H}_3\text{PO}_4 / \text{H}_2\text{PO}_4^-)$	2.16	12
Second dissociation, $\text{p}K_{a,2} (\text{H}_2\text{PO}_4^- / \text{HPO}_4^{2-})$	7.20	12
Third dissociation, $\text{p}K_{a,3} (\text{HPO}_4^{2-} / \text{PO}_4^{3-})$	12.36	12
Universal gas constant	$8.314 \text{ J} (\text{mol}\cdot\text{K})^{-1}$	9
Temperature of reaction	293.15 K	This work

Supporting figures, tables, and schemes

Mass transfer characterization of the electrochemical flow cell

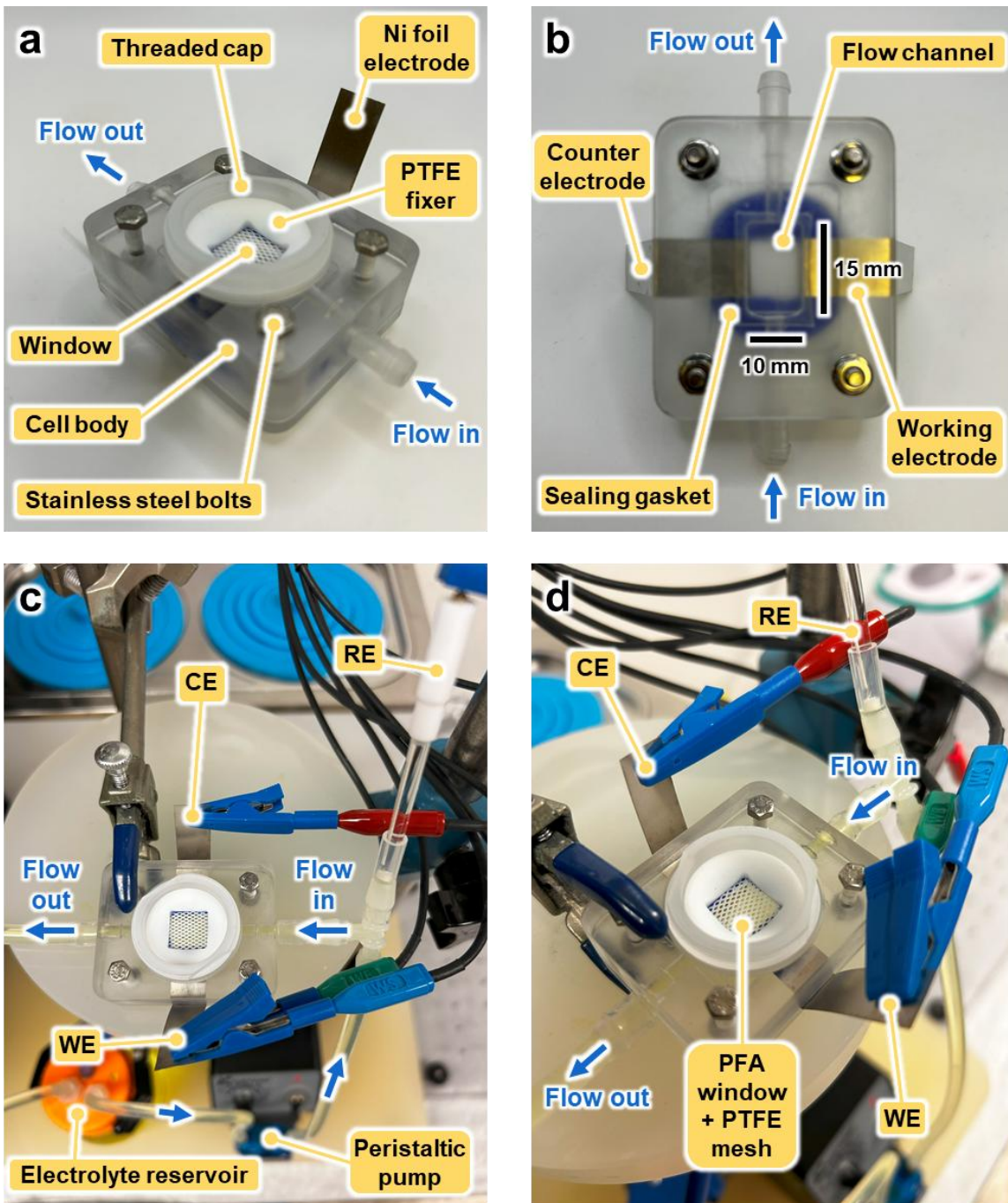


Figure S1. Experimental setup for characterizing the mass transport properties of the CFRS flow cell: (a) photograph of the assembled flow cell and its components, (b) bottom view of the flow cell highlighting the flow channel, (c) view of the flow system configured for ferricyanide reduction, and (d) close-up of the flow cell during mass transport characterization tests.

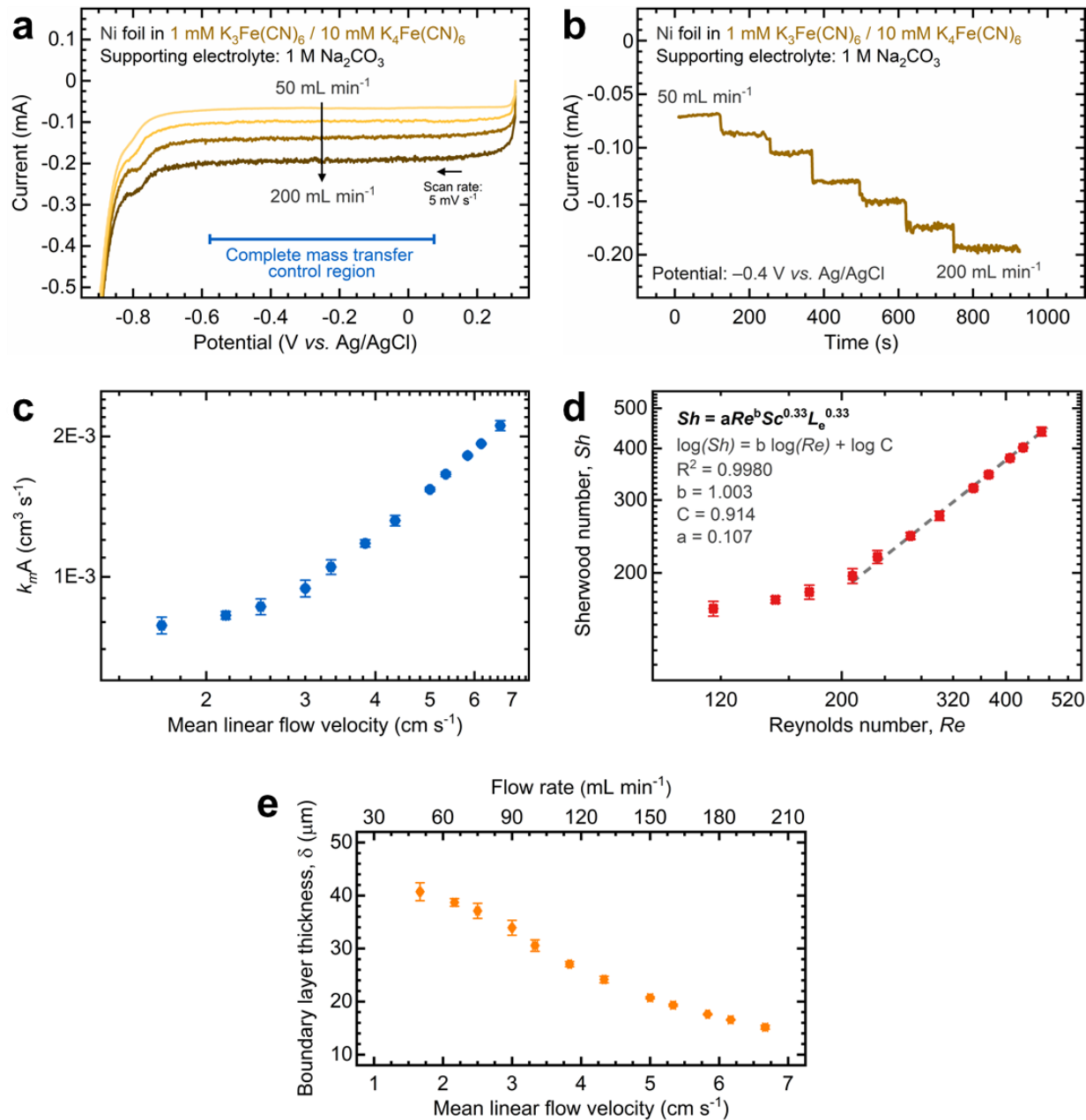


Figure S2. Mass transport characterization of the CFRS flow cell: (a) Linear sweep voltammograms of ferricyanide reduction under complete mass transport conditions at increasing flow rates, (b) steady-state ferricyanide reduction tests conducted via multistep chronoamperometry at increasing flow rates, (c) plot of the mass transport coefficient-area product as a function of mean linear flow velocity, (d) Sherwood number as a function of the Reynolds number. The dashed line represents the linear fit of the logarithmic function displayed. (e) Boundary layer thickness, estimated from the mass transport coefficient (Eq. 7), as a function of mean linear flow velocity and flow rate. Uncertainty bars indicate the standard deviation derived from three replicate measurements. Additional experimental conditions: Ni foil electrodes (geometric area: 0.5 cm²), 1 M Na_2CO_3 supporting electrolyte at 20 °C.

In-line CFRS experiments using PMP electrolyte under alkaline conditions

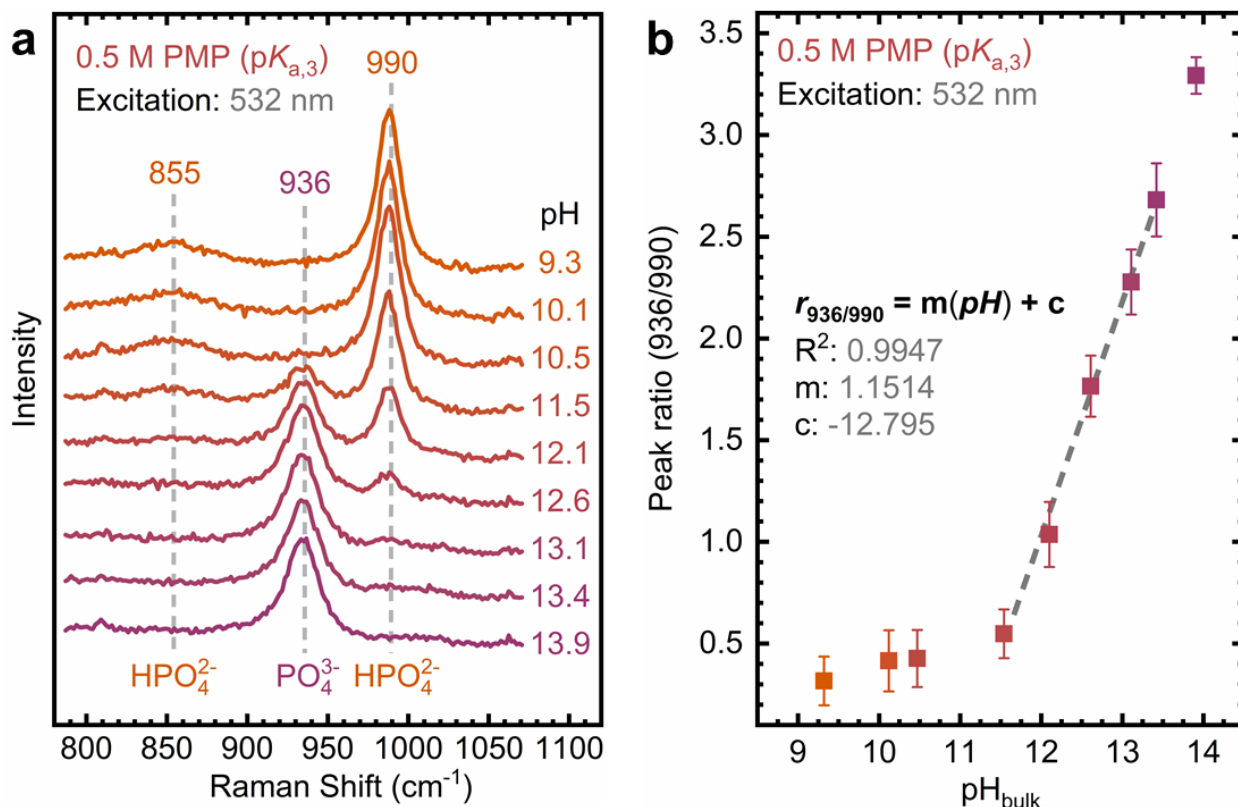


Figure S3. Calibration curve of the phosphate molecular probe under alkaline pH conditions ($pK_{a,3} = 12.36$): (a) Raman spectra recorded at varying pH values, and (b) plot of the phosphate/monohydrogen phosphate peak ratio as a function of bulk pH. The dashed line in (b) represents the linear fit of the displayed function. The calibration curve is valid within the range where both phosphate and monohydrogen phosphate peaks concur. Additional experimental conditions: Spectra were collected using the flow cell loaded with PMP electrolyte at 20 °C and OCP. The pH was adjusted using 3 M HNO_3 or 3 M KOH as needed. Data were collected with the laser beam positioned at the center of the flow channel (nominally 5 mm from each electrode). Flow rate: 100 $\text{mL}\cdot\text{min}^{-1}$.

Supporting Note: The calibration curve is linear within the region where both PO_4^{3-} and HPO_4^{2-} bands at 939 and 990 cm^{-1} are visible.

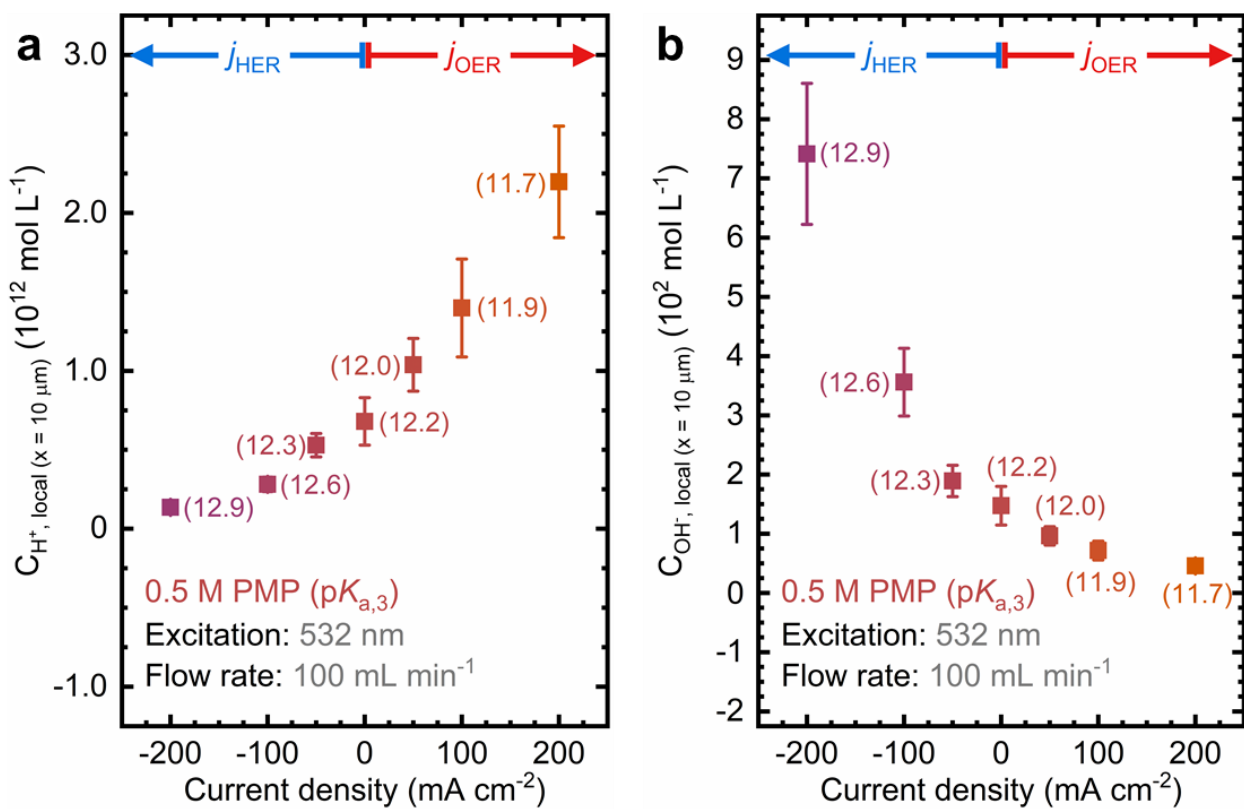


Figure S4. Local (a) H^+ and (b) OH^- concentrations as a function of the applied current density for in-line CFRS measurements using the phosphate molecular probe under alkaline pH conditions ($pK_{a,3} = 12.36$). Corresponding pH values are shown in parentheses. Data were collected with the laser beam located nominally 10 μm from the electrode surface. The scale on the y-axis was multiplied by a factor of 10^{12} in (a) and 10^2 in (b).

Supporting Note: The local H^+ concentration was calculated from the experimental local pH, obtained via the in-line CFRS technique, by using **Eq. S75**:

$$C_{H^+ \text{ local}} = 10^{-pH_{\text{local}}} \quad (\text{S75})$$

The local OH^- concentration was calculated from the local pOH using **Eq. S76**:

$$C_{OH^- \text{ local}} = 10^{-pOH_{\text{local}}} \quad (\text{S76})$$

where $pOH_{\text{local}} = 14 - pH_{\text{local}}$.

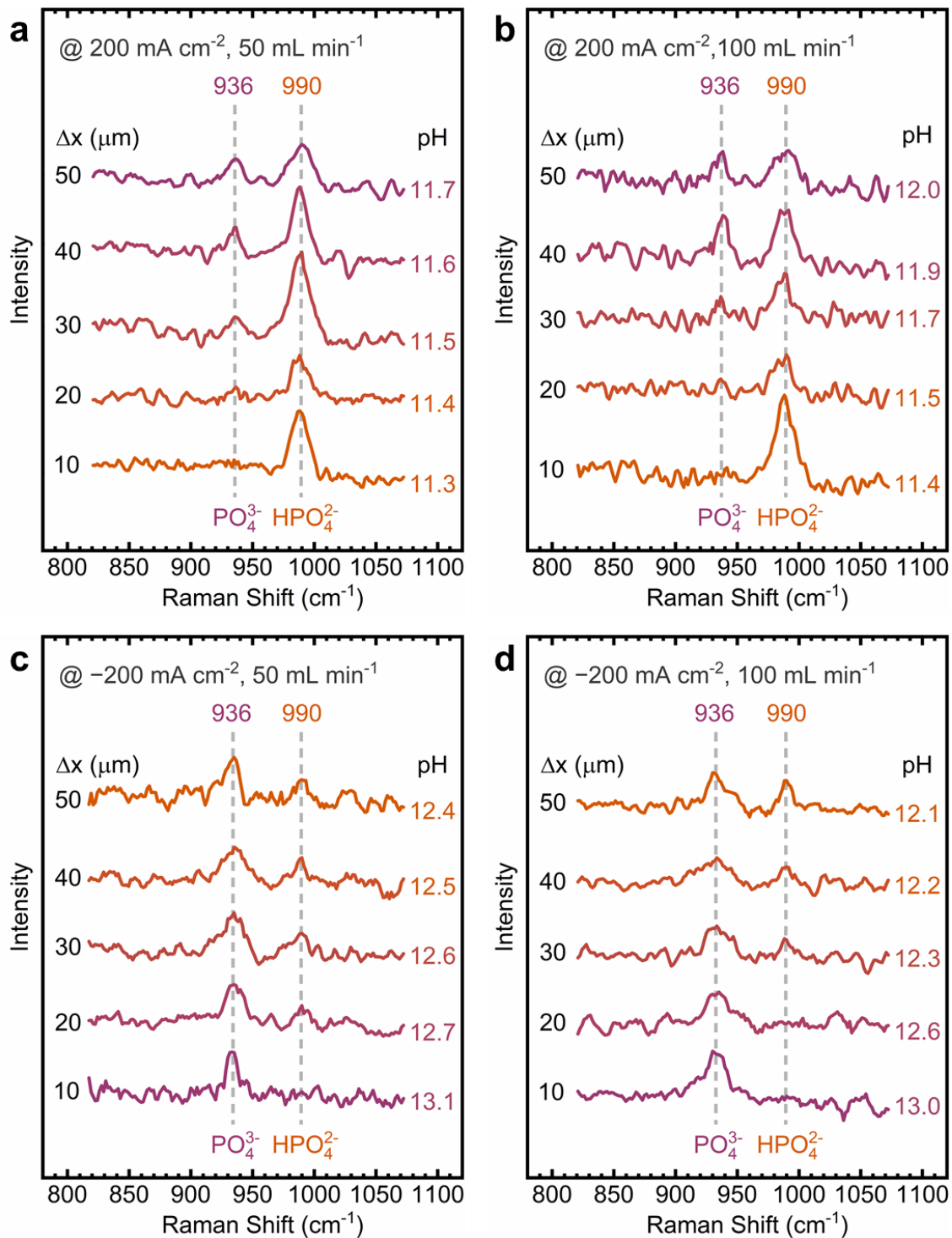


Figure S5. Raman spectra collected during location-dependent local pH tests under alkaline pH conditions: Spectra collected under OER current densities at a flow rate of (a) 50 and (b) $100 \text{ mL}\cdot\text{min}^{-1}$. Spectra collected under HER current densities at a flow rate of (c) 50 and (d) $100 \text{ mL}\cdot\text{min}^{-1}$. The spectra are stacked to reflect increasing distances from the electrode surface, with corresponding pH values estimated using the calibration curve for PMP electrolyte at alkaline pH (Figure S3).

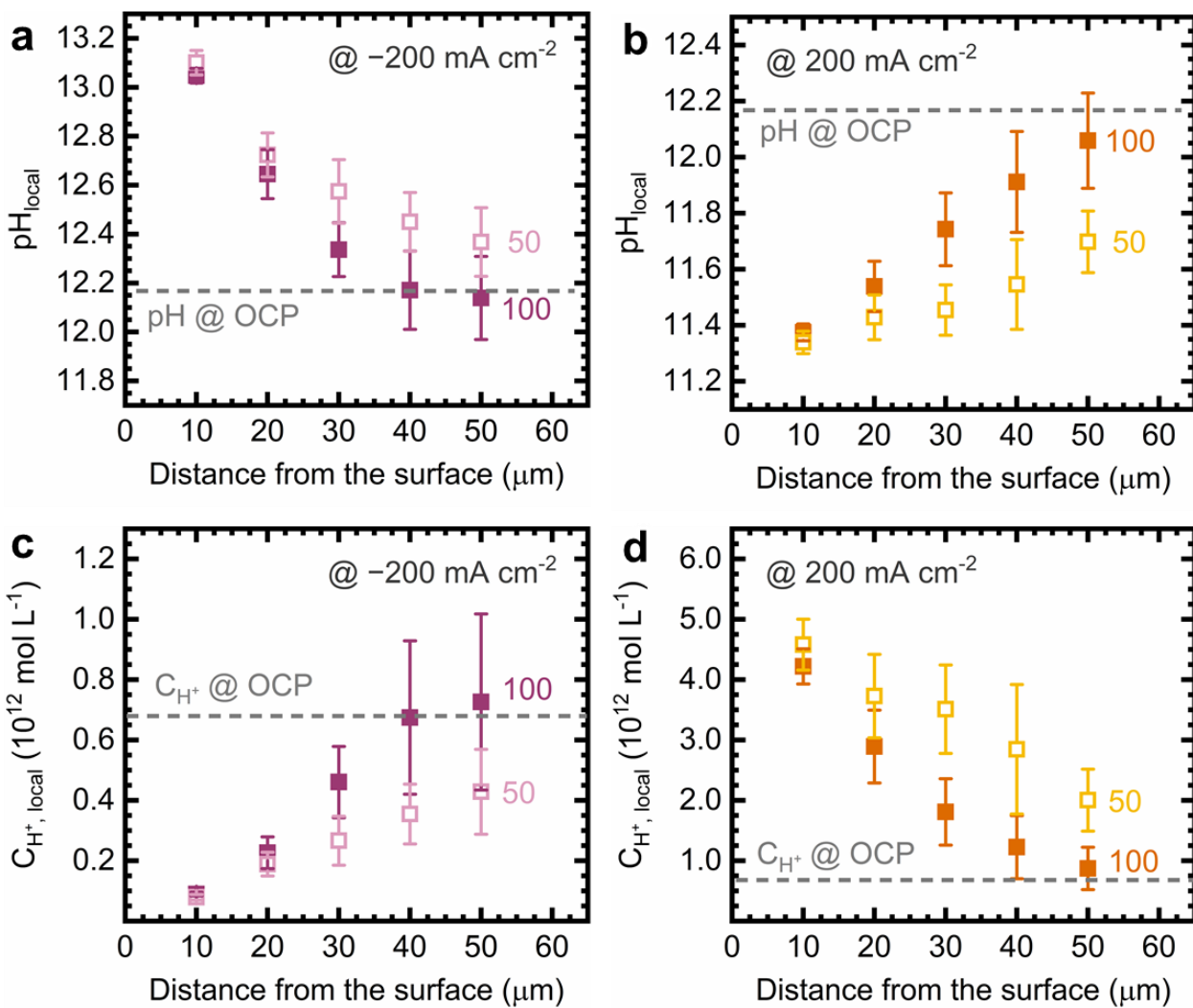


Figure S6. Local pH profiles as a function of distance from the electrode surface under (a) HER and (b) OER current densities. Local H^+ concentration as a function of distance from the electrode surface under (c) HER and (d) OER current densities. Measurements were performed on the 0.5 M PMP system under alkaline conditions ($\text{pK}_{\text{a},3} = 12.36$) at flow rates of 50 and 100 $\text{mL}\cdot\text{min}^{-1}$. Horizontal dashed lines indicate the pH (or H^+ concentration) estimated from Raman peak intensities measured at OCP. Uncertainty bars indicate the standard deviation derived from three replicate measurements. The scale on the y-axis for (c) and (d) was multiplied by a factor of 10^{12} .

Supporting Note: The local H^+ concentration was calculated from the experimental local pH, obtained via the in-line CFRS technique, using Eq. S75.

In-line CFRS experiments using PMP electrolyte under near-neutral conditions

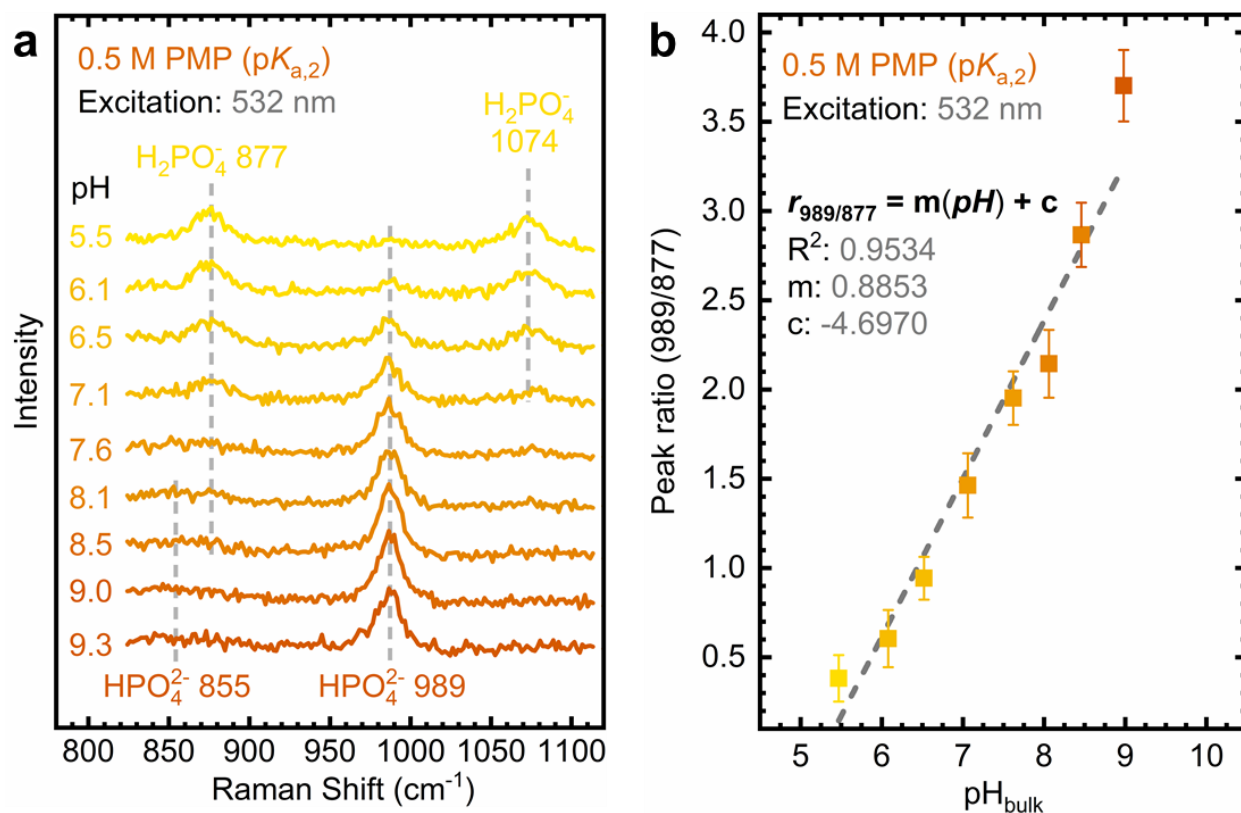


Figure S7. Calibration curve of the phosphate molecular probe under near-neutral conditions ($pK_{a,2} = 7.20$): (a) Raman spectra recorded at varying pH values, and (b) plot of the monohydrogen phosphate/dihydrogen phosphate peak ratio as a function of bulk pH. The dashed line in (b) represents the linear fit of the displayed function. The calibration curve is valid within the range where monohydrogen phosphate and dihydrogen phosphate peaks concur. Additional experimental conditions: Spectra were collected using the flow cell loaded with PMP electrolyte at 20 °C and OCP. The pH was adjusted using 3 M HNO₃ or 3 M KOH as needed. Data were collected with the laser beam positioned at the center of the flow channel (nominally 5 mm from each electrode). Flow rate: 100 mL·min⁻¹.

Supporting Note: The calibration curve is linear within the region where both HPO_4^{2-} and $H_2PO_4^-$ bands at 989 and 877 cm^{-1} are visible.

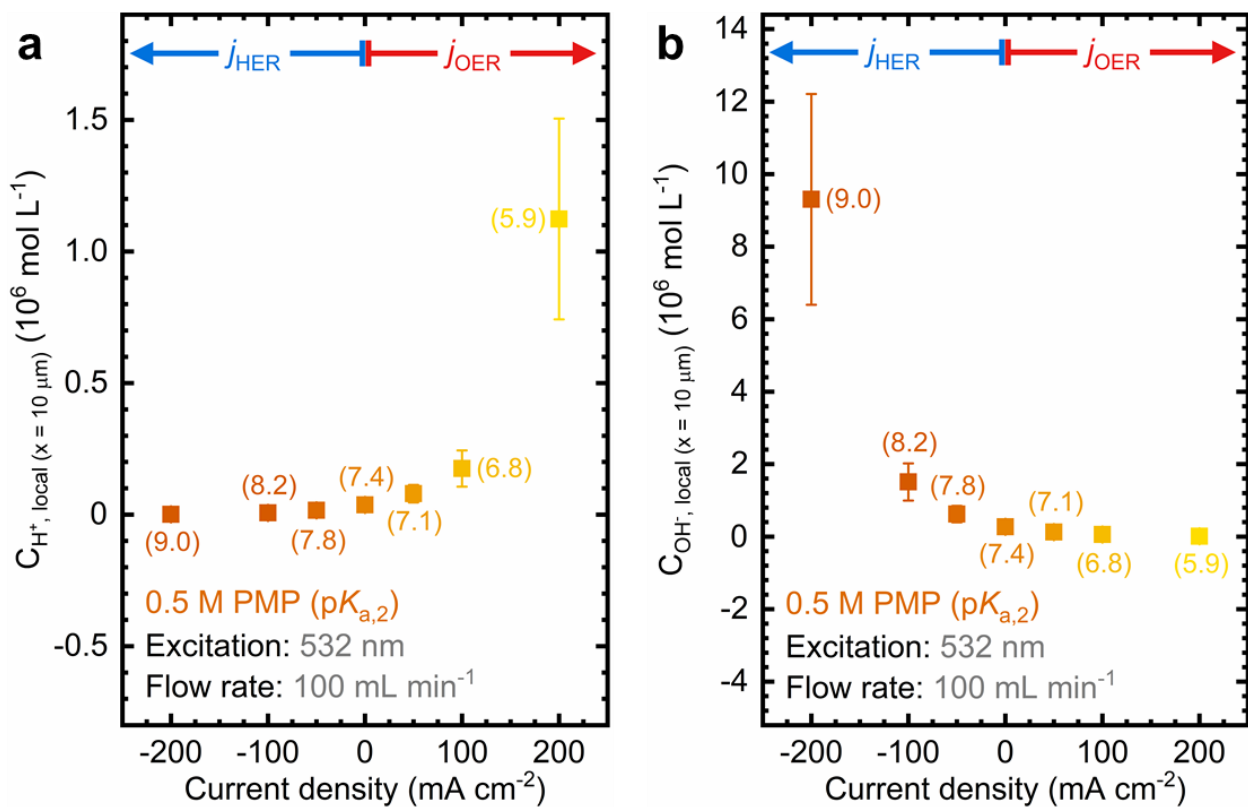


Figure S8. Local (a) H^+ and (b) OH^- concentrations as a function of the applied current density for in-line CFRS measurements using the phosphate molecular probe under near-neutral conditions ($pK_{a,2} = 7.20$). Corresponding pH values are shown in parentheses. Data were collected with the laser beam located nominally $10 \mu\text{m}$ from the electrode surface. The scale on the y-axis was multiplied by a factor of 10^6 in both plots.

Supporting Note: The local H^+ and OH^- concentrations were calculated from the experimental local pH, obtained via the in-line CFRS technique, using **Eqs. S75 and S76**.

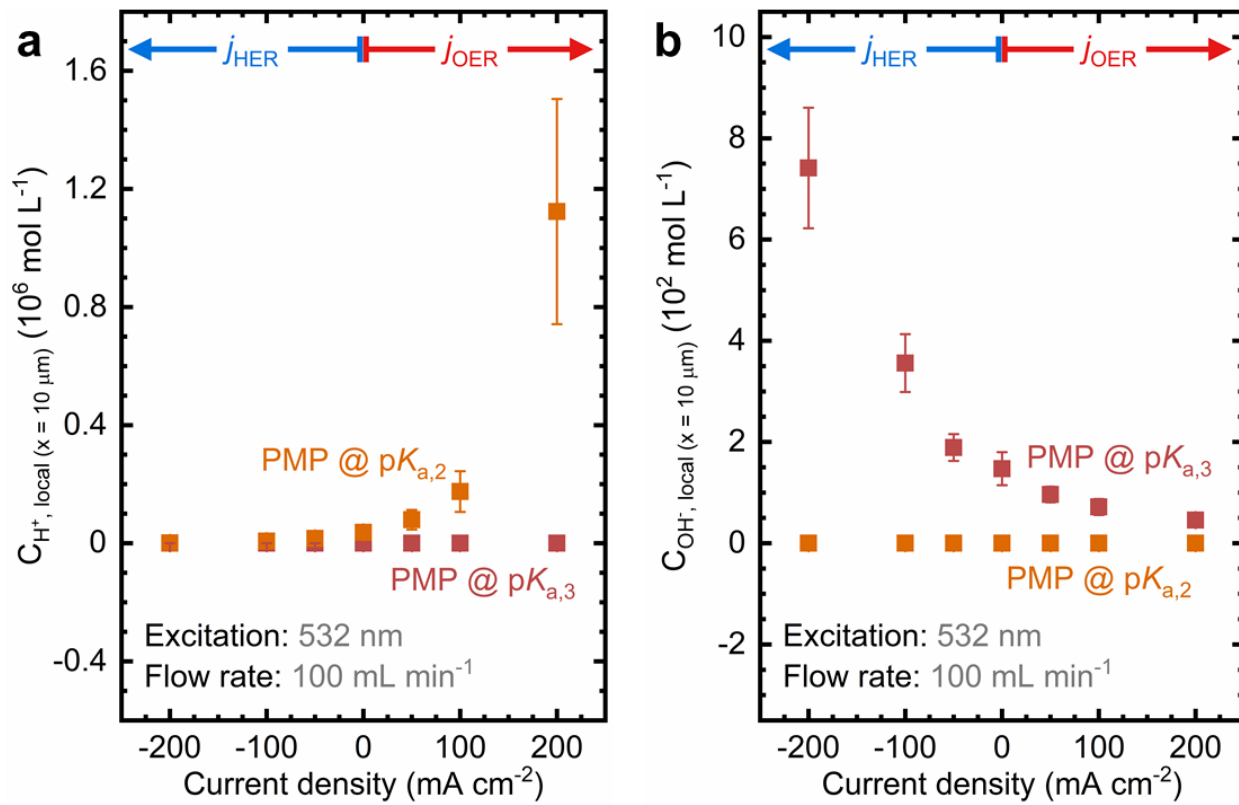


Figure S9. Magnitude of local (a) H^+ and (b) OH^- concentrations as a function of the applied current density for the in-line CFRS technique using the phosphate molecular probe. Data were collected with the laser beam located nominally $10 \mu\text{m}$ from the electrode surface. The scale on the y-axis was multiplied by a factor of 10^6 in (a) and 10^2 in (b).

Supporting Note: The local H^+ and OH^- concentrations were calculated from the experimental local pH, obtained via the in-line CFRS technique, using **Eqs. S75 and S76**.

Analytical modeling of interfacial pH swings

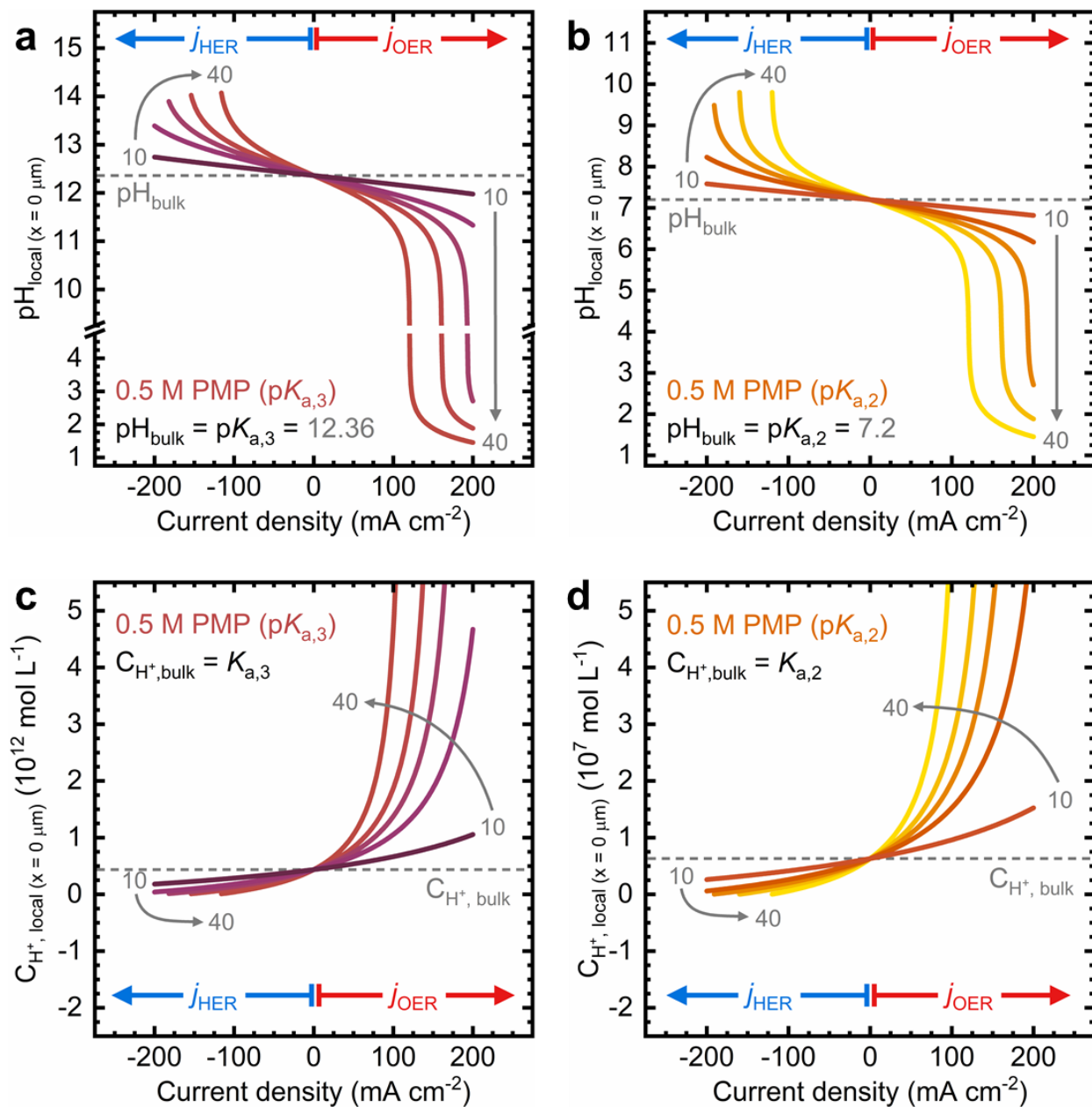


Figure S10. Local pH as a function of the current density for the phosphate molecular probe at (a) $\text{p}K_{\text{a},3}$ and (b) $\text{p}K_{\text{a},2}$ using the local pH model proposed by the Nocera Group.¹¹ Corresponding local H^+ concentration plots for (c) $\text{p}K_{\text{a},3}$ and (d) $\text{p}K_{\text{a},2}$ are included. Horizontal dashed lines represent the bulk pH/ H^+ concentration for phosphate buffer at the corresponding $\text{p}K_{\text{a}}$ value. The pH and H^+ concentration profiles are plotted at increasing boundary layer thickness (10, 20, 25, 30, and 40 μm). Parameters obtained from this model refer to the electrode surface ($x = 0$). The constants used to plot these pH profiles are shown in **Table S2**.

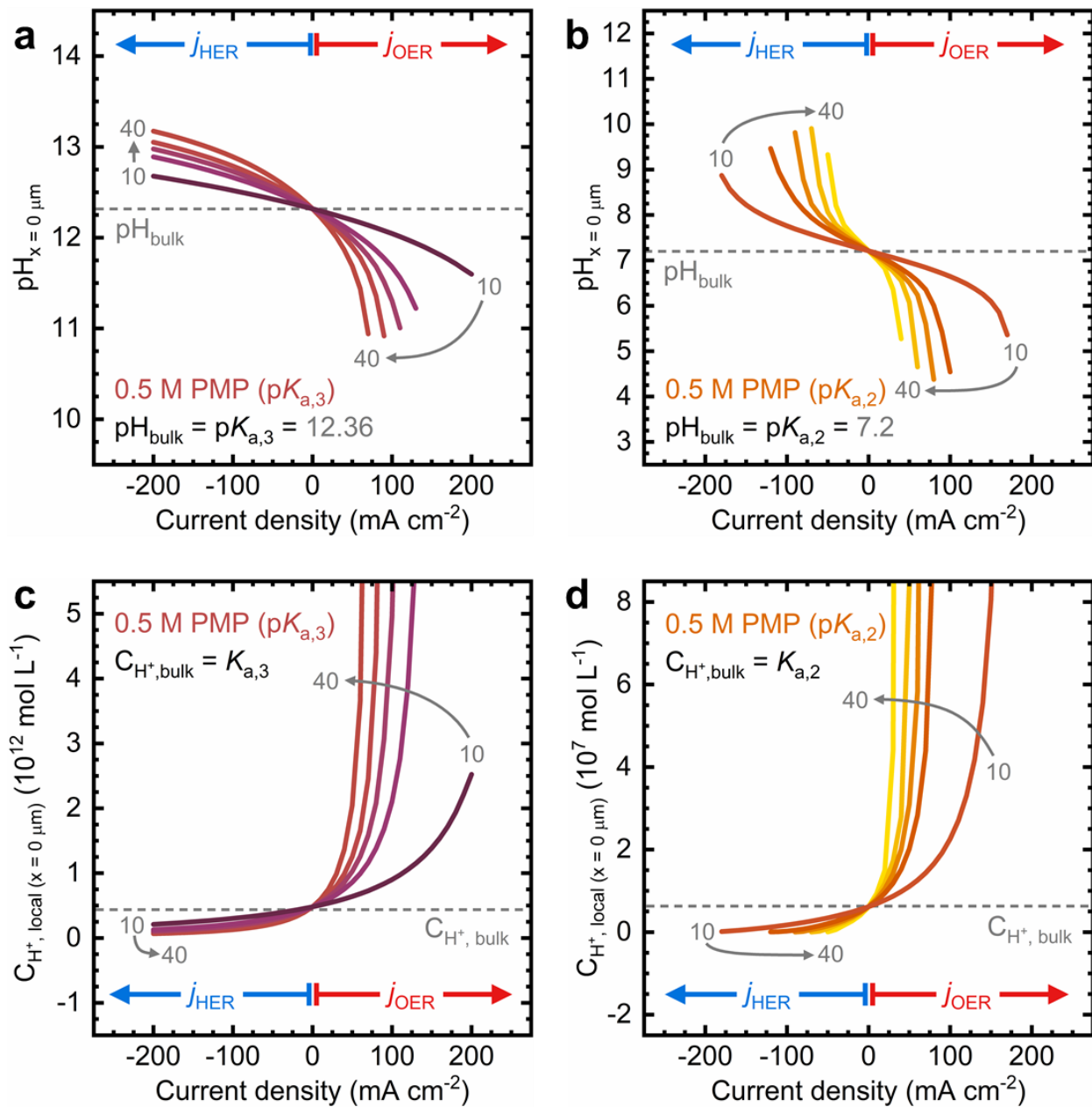


Figure S11. Local pH as a function of the current density for the phosphate molecular probe at (a) $\text{pK}_{\text{a},3}$ and (b) $\text{pK}_{\text{a},2}$ using the local pH model built in COMSOL Multiphysics. Corresponding local H^+ concentration plots for (c) $\text{pK}_{\text{a},3}$ and (d) $\text{pK}_{\text{a},2}$ are included. Horizontal dashed lines represent the bulk pH/ H^+ concentration for phosphate buffer at the corresponding pK_α value. The pH and H^+ concentration profiles are plotted at increasing boundary layer thickness (10, 20, 25, 30, and 40 μm). Parameters obtained from this model refer to the electrode surface ($x = 0$). The constants used to plot these pH profiles are shown in **Table S3**.

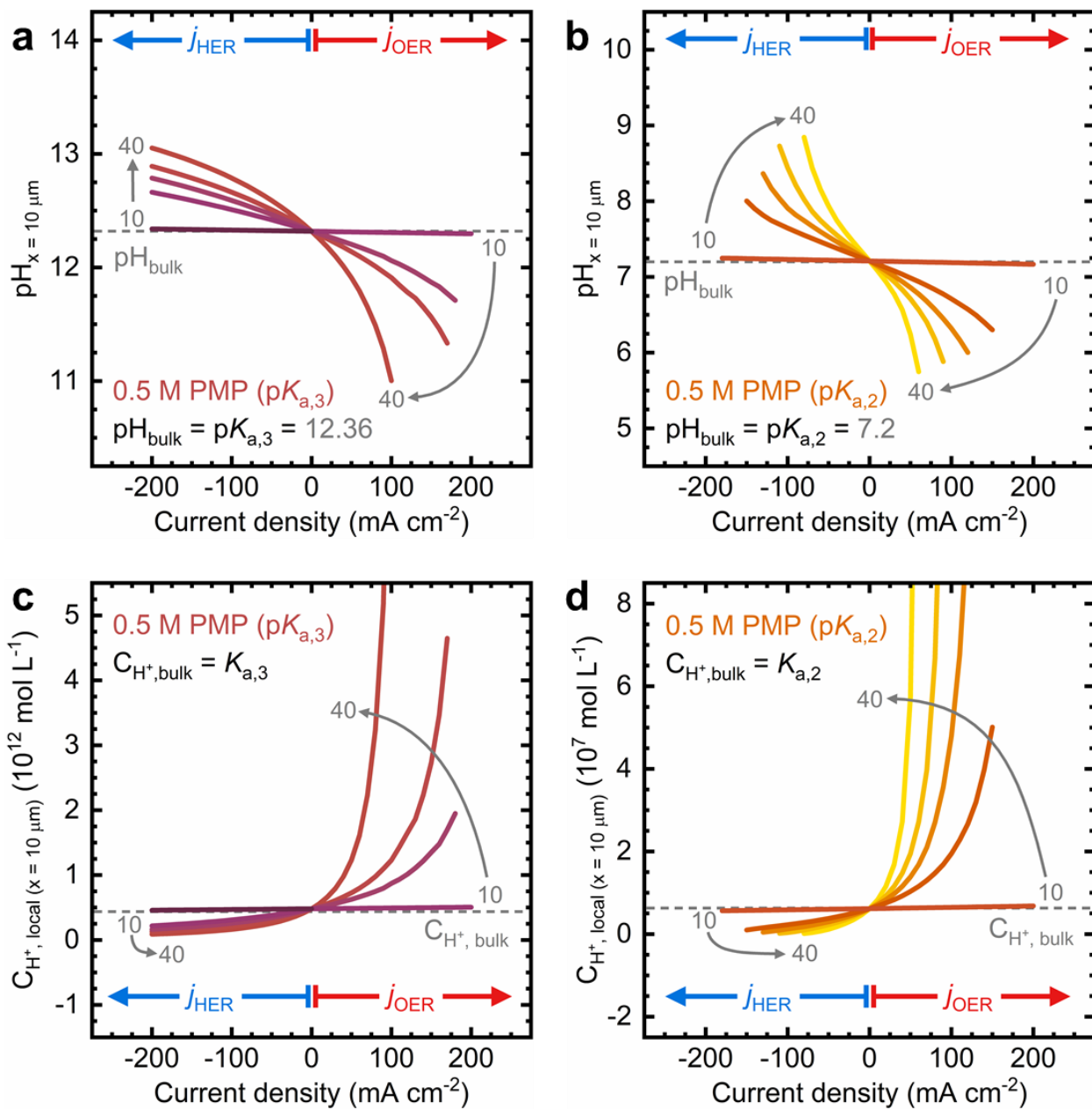


Figure S12. Local pH as a function of the current density for the phosphate molecular probe at (a) $\text{p}K_{a,3}$ and (b) $\text{p}K_{a,2}$ using the local pH model built in COMSOL Multiphysics. Corresponding local H^+ concentration plots for (c) $\text{p}K_{a,3}$ and (d) $\text{p}K_{a,2}$ are included. Horizontal dashed lines represent the bulk pH/ H^+ concentration for phosphate buffer at the corresponding $\text{p}K_a$ value. The pH and H^+ concentration profiles are plotted at increasing boundary layer thickness (10, 20, 25, 30, and 40 μm). Parameters obtained from this model refer to a distance of 10 μm from the electrode surface. The constants used to plot these pH profiles are shown in **Table S3**.

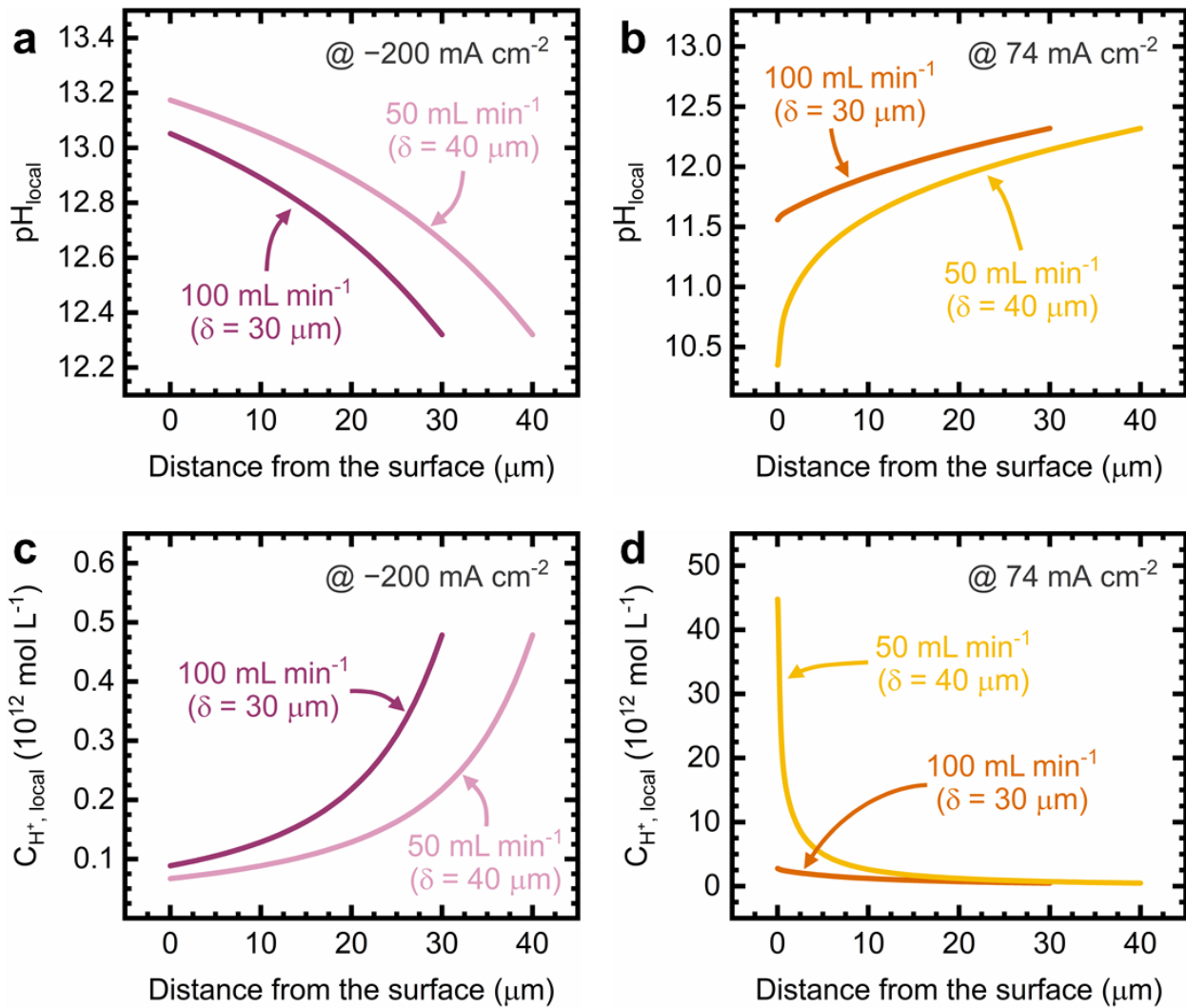


Figure S13. Local pH as a function of distance from the electrode surface under: (a) HER and (b) OER current densities, estimated using the local pH model built in COMSOL Multiphysics for the 0.5 M PMP system under alkaline conditions ($\text{pK}_{\text{a},3} = 12.36$). Corresponding local H^+ concentration plots for (c) HER and (d) OER current densities are included. The pH and H^+ concentration profiles are plotted at two boundary layer thicknesses (30 and 40 μm), corresponding to the experimental flow rates of the in-line CFRS technique (50 and 100 $\text{mL}\cdot\text{min}^{-1}$, **Figure S2e**). Parameters obtained from this model refer to a distance of 10 μm from the electrode surface. The constants used to generate these plots are shown in **Table S3**.

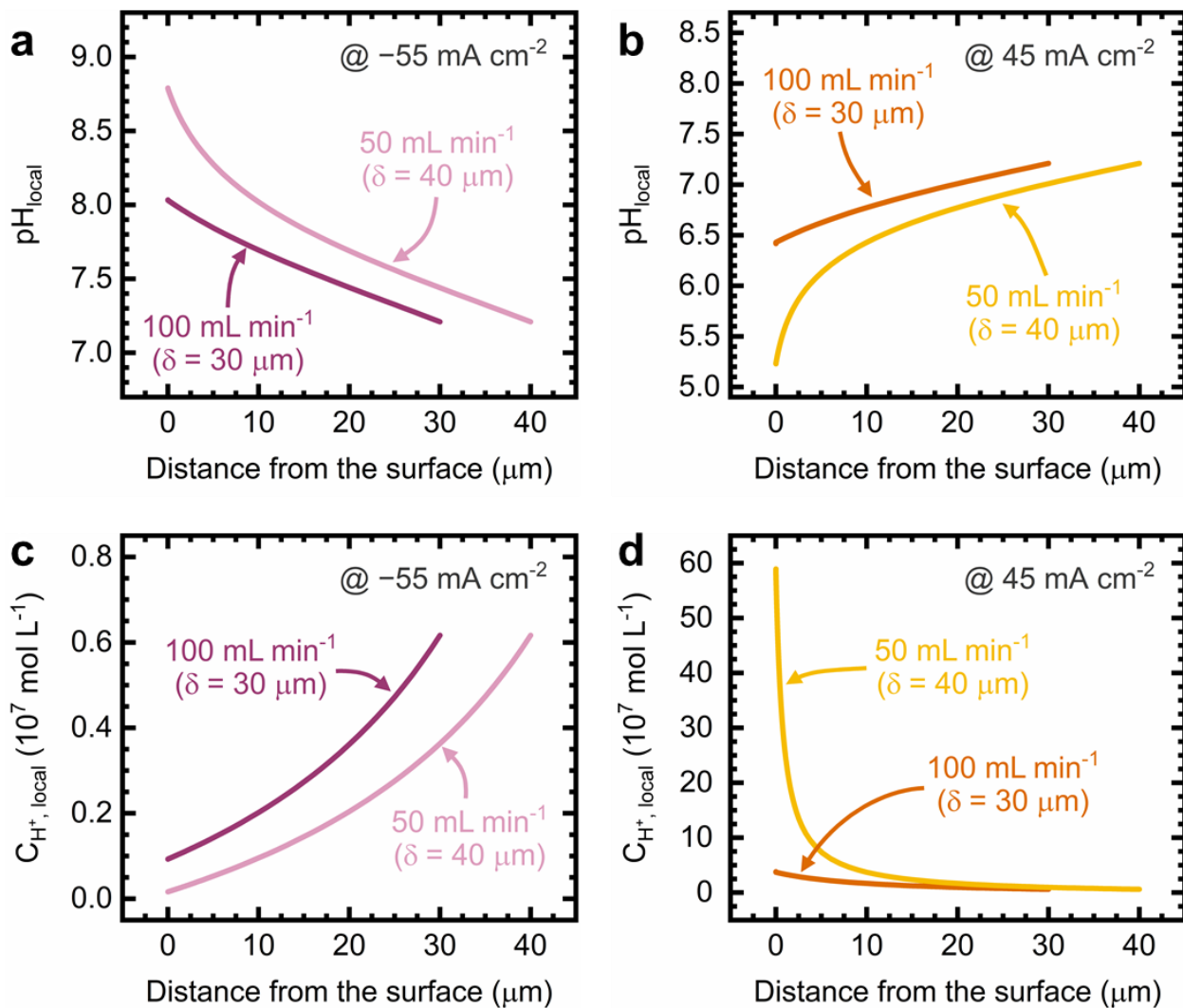


Figure S14. Local pH as a function of distance from the electrode surface under: (a) HER and (b) OER current densities, estimated using the local pH model built in COMSOL Multiphysics for the 0.5 M PMP system under near-neutral conditions ($\text{p}K_{\text{a},2} = 7.20$). Corresponding local H^+ concentration plots for (c) HER and (d) OER current densities are included. The pH and H^+ concentration profiles are plotted at two boundary layer thicknesses (30 and 40 μm), corresponding to the experimental flow rates of the in-line CFRS technique (50 and 100 mL min^{-1} , **Figure S2e**). Parameters obtained from this model refer to a distance of 10 μm from the electrode surface. The constants used to generate these plots are shown in **Table S3**.

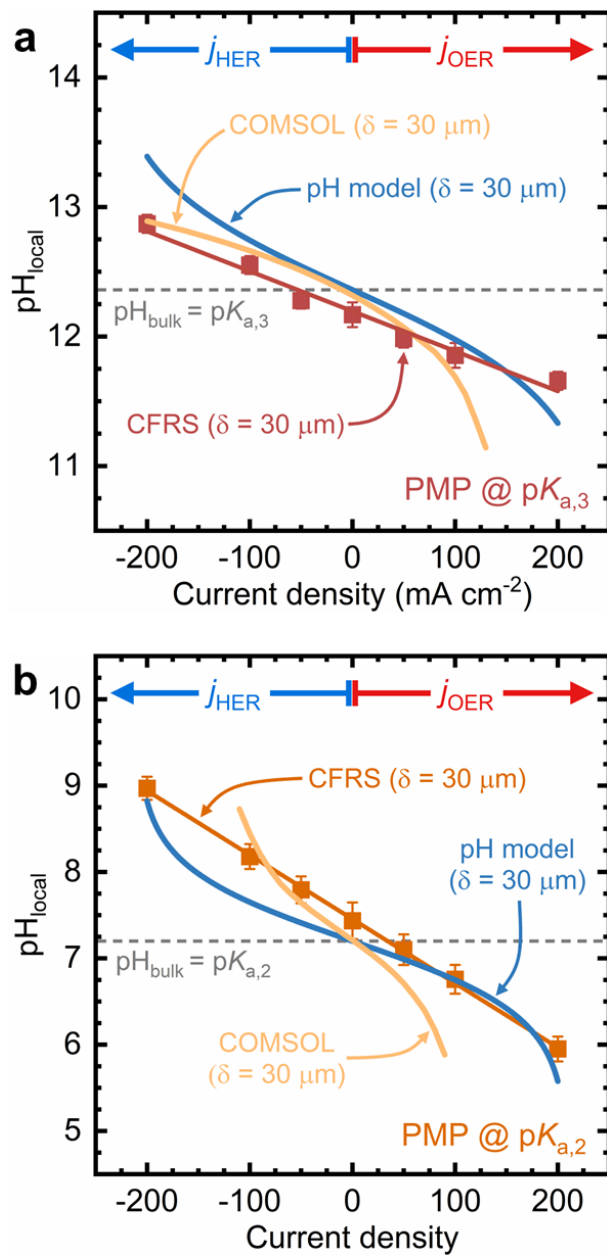


Figure S15. Magnitude of local pH changes as a function of the applied current density for the phosphate molecular probe at (a) $pK_{a,3}$ and (b) $pK_{a,2}$. Experimental results from the in-line CFRS technique are contrasted with local pH profiles derived from the pH model proposed by the Nocera Group and our continuum model built in COMSOL Multiphysics. The boundary layer thickness (δ) is shown in parentheses and equals $30 \mu\text{m}$ for all scenarios. Local pH values were calculated at $10 \mu\text{m}$ from the electrode surface for the experimental CFRS method and COMSOL model. The horizontal dashed line shows the bulk pH for the PMP electrolyte at its pK_a as a reference.

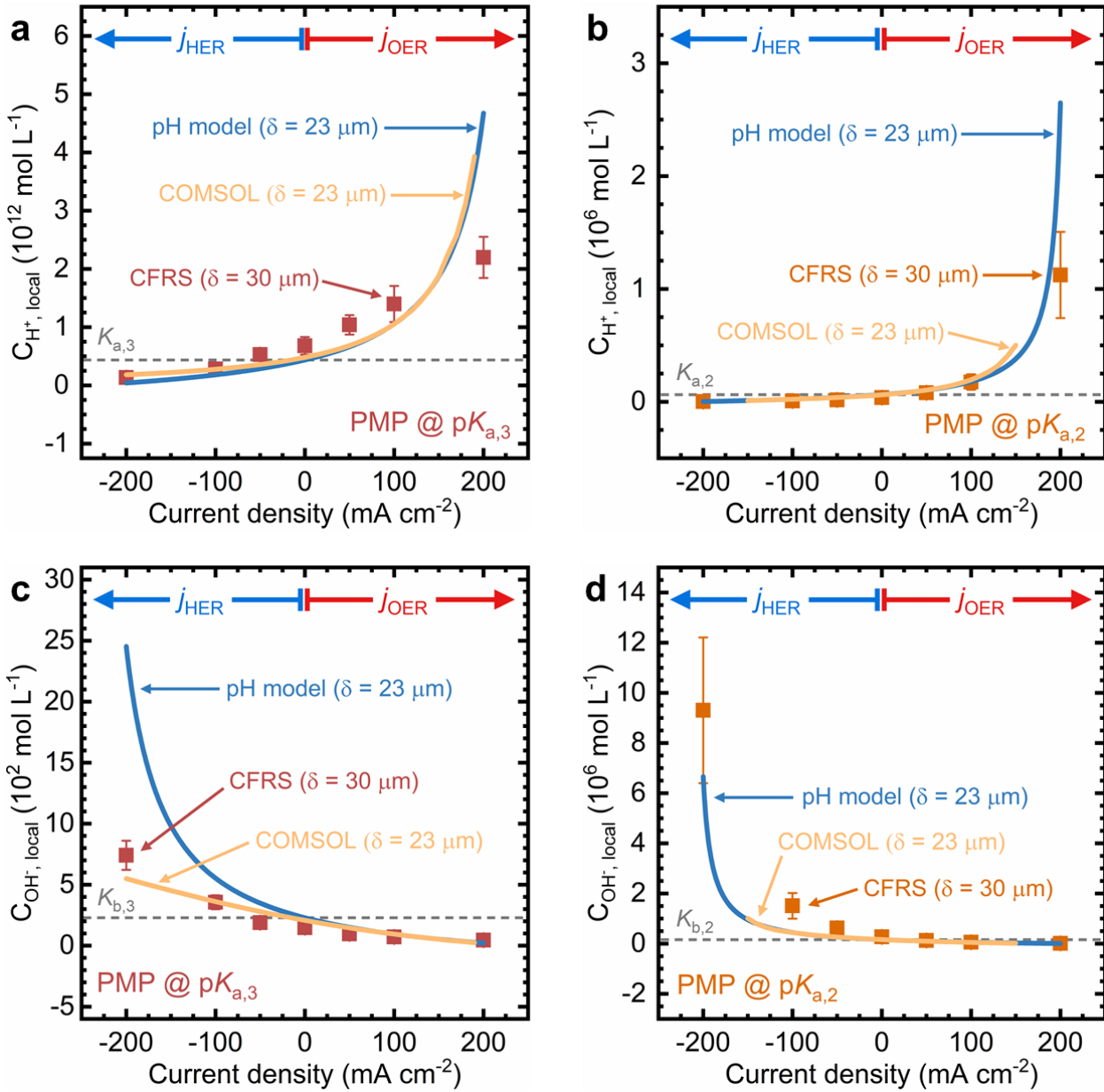


Figure S16. Magnitude of local H^+ concentrations as a function of the applied current density for the phosphate molecular probe at (a) $pK_{a,3}$ and (b) $pK_{a,2}$. Magnitude of local OH^- concentrations as a function of the applied current density for the phosphate molecular probe at (c) $pK_{a,3}$ and (d) $pK_{a,2}$. Experimental results from the in-line CFRS technique are contrasted with local H^+ and OH^- concentrations derived from the pH model proposed by the Nocera Group and our continuum model built in COMSOL Multiphysics. The boundary layer thickness (δ) is shown in parentheses. Local ion concentrations were calculated at 10 μm from the electrode surface for the experimental CFRS method and our continuum model. The horizontal dashed lines in (a) and (b) show the bulk H^+ concentrations for the PMP electrolyte at its K_a as a reference. Dashed lines for (c) and (d) show the bulk OH^- concentrations at K_b .

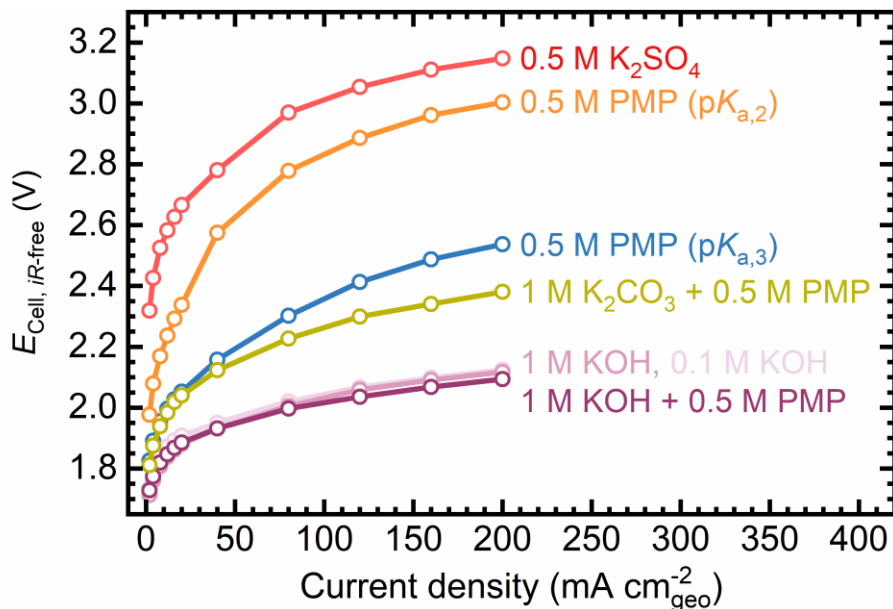


Figure S17. Full-cell polarization curves for different near-neutral and alkaline electrolytes tested during in-line CFRS measurements. The cell potential was corrected for the total iR drop using galvanostatic EIS (details below). Each data point represents the average potential from multistep chronopotentiometry runs. Measurements were performed in the same flow cell used for in-line CFRS experiments at a flow rate of $100 \text{ mL}\cdot\text{min}^{-1}$ and 20°C . Additional performance metrics extracted from the polarization curves and EIS are shown in **Table S4**.

Supporting note: Although electrochemical performance is not the primary focus of this study, polarization curves and EIS data for various electrolytes are provided to highlight differences in their electrochemical behavior. Multistep CP runs were used to construct full-cell polarization curves. Each constant current step lasted 300 s, followed by galvanostatic EIS at the same current. Average cell voltages were derived from the final 60 s of each step. Galvanostatic EIS was used to measure the high-frequency resistance (HFR), which accounts for the ion conduction resistance, R_{ion} , from the electrolyte, and the electronic resistance, R_{el} , from the electrode:²³

$$\text{HFR} = R_{\text{ion}} + R_{\text{el}} \quad (\text{S77})$$

Galvanostatic EIS was conducted at $15 \text{ mA}\cdot\text{cm}^{-2}$, with an AC amplitude of 5 mA over a frequency range of 100 kHz to 1 Hz, with drift correction enabled. The HFR was obtained

from the high-frequency intercept of the Nyquist plot with the real axis.²⁴ Next, the HFR measured at each step was used to calculate the *iR*-corrected potential, $E_{\text{Cell}, iR\text{-free}}$, for each corresponding cell voltage, E_{cell} , based on Eq. 78:²⁴

$$E_{\text{Cell}, iR\text{-free}} = E_{\text{cell}} - i \cdot \text{HFR} \quad (\text{S78})$$

where i is the current applied at each step. **Table S4** summarizes electrochemical performance metrics for each electrolyte.

Table S4. Electrochemical metrics for different electrolytes tested in the CFRS flow cell.

Electrolyte	Bulk pH	HFR @ 15 mA·cm ⁻² from EIS (Ω)	$E_{\text{Cell}, iR\text{-free}} @ 100$ mA·cm ⁻² (V)
1 M KOH + 0.5 M PMP ($\text{p}K_{\text{a},3}$)	13.99	5.60 ± 0.01	2.019
1 M KOH	13.99	6.54 ± 0.04	2.028
0.1 M KOH	13.23	55.80 ± 3.33	2.045
0.5 M PMP ($\text{p}K_{\text{a},3}$)	12.33	16.32 ± 0.13	2.355
1 M K_2CO_3 + 0.5 M PMP ($\text{p}K_{\text{a},3}$)	11.87	7.50 ± 0.02	2.261
0.5 M PMP ($\text{p}K_{\text{a},2}$)	7.43	22.99 ± 0.12	2.832
0.5 M K_2SO_4	7.36	30.04 ± 0.47	3.010

The uncertainty indicates the standard deviation derived from five EIS measurements.

Results from **Figure S17** and **Table S4** suggest that adding phosphate species has minimal impact on the catalytic performance of water-splitting reactions. For example, after extracting the HFR, the 1 M KOH and 1 M KOH + 0.5 PMP electrolytes exhibit nearly identical performance. Note that the 0.5 PMP electrolyte alone shows higher overpotentials than 0.1 M KOH. Except for the carbonate-containing electrolyte, the cell potential decreases as the solution pH increases, indicating that the OH^- concentration likely limits catalytic performance. These results suggest that the PMP does not influence the catalytic performance significantly, at least under the conditions used for in-line CFRS measurements (i.e., high current densities, Pt electrodes, room temperature).

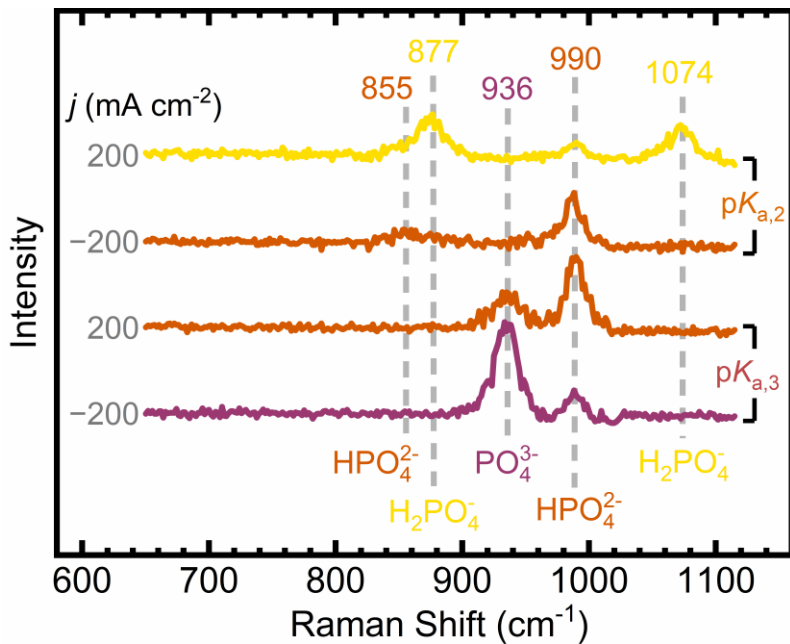


Figure S18. Raman spectra collected during in-line CFRS experiments under alkaline ($pK_{a,3}$) and near-neutral ($pK_{a,2}$) conditions at high current densities used to determine the signal-to-noise ratio (SNR), limit of detection (LOD), and limit of quantitation (LOQ). Dashed lines indicate the peak position for the corresponding species from the PMP electrolyte. Data were collected with the laser beam located nominally 10 μm from the electrode surface. Flow rate: 100 $\text{mL}\cdot\text{min}^{-1}$.

Supporting note: The signal-to-noise ratio (SNR) and limit of detection (LOD) were estimated at high current densities, where one of the peaks used for calculating the peak ratio decreases significantly and may be obscured by background noise. The SNR was determined following guidelines from the Raman spectrometer's manufacturer:²⁵

$$\text{SNR} = \frac{S}{N} = \frac{y_i - y_b}{\sqrt{y_b}} \quad (\text{S79})$$

where S is the signal intensity, N is the noise intensity, y_i is the intensity at a certain peak of interest i , and y_b is the intensity of the background (i.e., at a spectrum range where no signal is present). The value of y_b was averaged within the 650 – 750 cm^{-1} range (**Figure S18**). The SNR was calculated for the Raman peaks used for estimating the local pH from calibration curves on 0.5 M PMP electrolytes (at $pK_{a,3}$ and $pK_{a,2}$). Results are shown in **Table S5**. This SNR estimation method was used in other control experiments at different electrolytes and concentrations (vide infra).

Table S5. SNR estimation from in-line CFRS measurements at high current densities.

Electrolyte	j (mA·cm ⁻²)	$y_{b,\text{mean}}$ @ 700 cm ⁻¹	Peak position (cm ⁻¹)	y_i @ peak	SNR
PMP 0.5 M (p $K_{a,3}$)	200	11.04	936	45.50 ± 0.96	10.37 ± 0.29
PMP 0.5 M (p $K_{a,3}$)	200	11.04	990	81.50 ± 1.50	21.20 ± 0.32
PMP 0.5 M (p $K_{a,3}$)	-200	8.86	936	99.00 ± 1.46	30.27 ± 0.49
PMP 0.5 M (p $K_{a,3}$)	-200	8.86	990	31.66 ± 1.08	7.66 ± 0.36
PMP 0.5 M (p $K_{a,2}$)	200	11.80	990	25.83 ± 0.97	4.09 ± 0.28
PMP 0.5 M (p $K_{a,2}$)	200	11.80	877	50.93 ± 1.72	11.39 ± 0.50
PMP 0.5 M (p $K_{a,2}$)	-200	10.44	990	59.52 ± 1.42	15.19 ± 0.44
PMP 0.5 M (p $K_{a,2}$)	-200	10.44	877	20.05 ± 0.28	2.97 ± 0.09

The uncertainty indicates the standard deviation derived from three replicate measurements.

The LOD was calculated using Eq. S80:²⁶

$$\text{LOD} = y_b + 3s_b \quad (\text{S80})$$

where s_b is the standard deviation of the noise signal. The value of y_b was averaged within the 650 – 750 cm⁻¹ region, and the value of s_b was obtained within the same range. The limit of quantitation (LOQ) can be used as a more rigorous threshold for ensuring precise quantitative measurements:²⁶

$$\text{LOQ} = y_b + 10s_b \quad (\text{S81})$$

Table S6 shows the LOD and LOQ for the studied electrolytes.

Table S6. LOD and LOQ values from in-line CFRS measurements at high current densities.

Electrolyte	Current density (mA·cm ⁻²)	$y_{b,\text{mean}}$ @ 700 cm ⁻¹	s_b	LOD	LOQ
PMP 0.5 M (p $K_{a,3}$)	200	11.04	1.80	16.45	29.05
PMP 0.5 M (p $K_{a,3}$)	-200	8.86	2.45	16.21	33.34
PMP 0.5 M (p $K_{a,2}$)	200	11.80	2.11	18.14	32.93
PMP 0.5 M (p $K_{a,2}$)	-200	10.40	1.88	16.08	29.24

Comparison of the LOD values (**Table S6**) with the lowest peak intensities (y_i) in **Table S5** shows that our method can clearly distinguish the weakest signal from the background even at the highest current density. Similarly, most peak intensities are above the LOQ, with only two measurements for the 0.5 M PMP electrolyte at $pK_{a,2}$ falling slightly below this threshold. The SNR for the lowest intensity peaks remains above the minimum threshold (SNR = 2–3) required to ensure reliable signal detection, as recommended elsewhere.²⁷ Note, however, that the SNR values for the 0.5 M PMP electrolyte at $pK_{a,2}$ are significantly lower than those at $pK_{a,3}$. Therefore, increasing the concentration above 0.5 M may be necessary to improve the SNR in near-neutral PMP electrolytes.

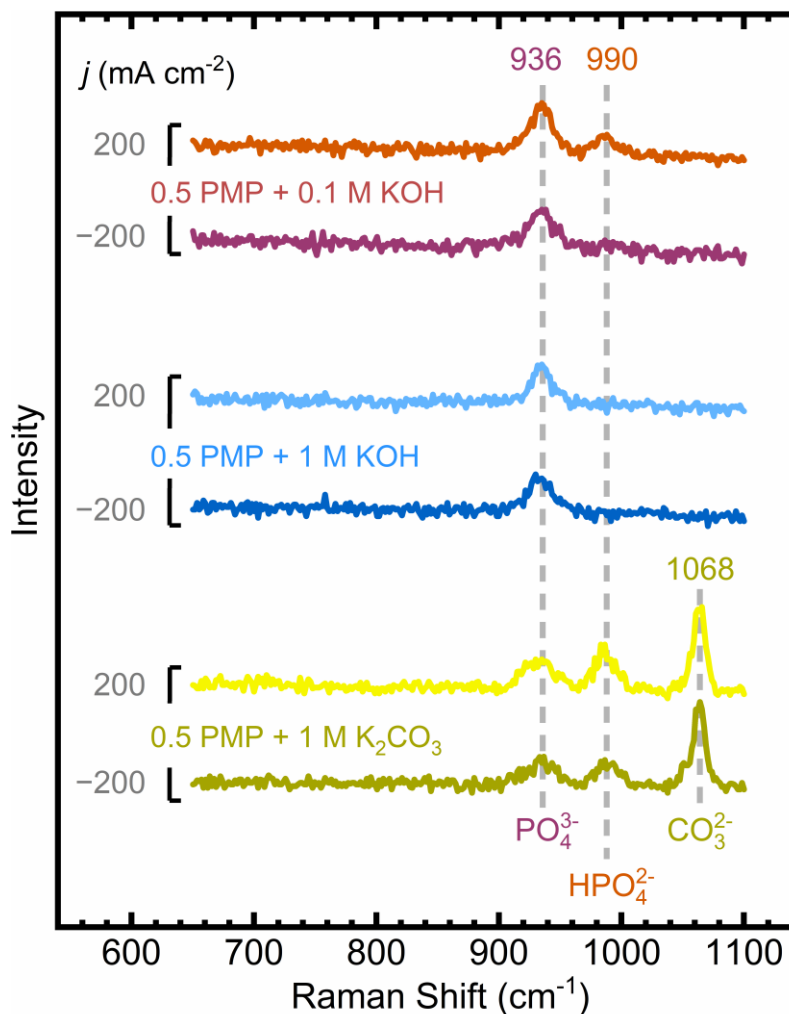


Figure S19. Raman spectra of alkaline electrolytes containing 0.5 M PMP ($pK_{a,3}$), collected during in-line CFRS experiments under high current density conditions. Dashed lines indicate the peak position for the corresponding species from the PMP electrolyte, along with the CO_3^{2-} band observed only in the K_2CO_3 -containing electrolyte. Data were collected with the laser beam located nominally 10 μm from the electrode surface. Flow rate: 100 $\text{mL}\cdot\text{min}^{-1}$.

Supporting note: PMP was added to other alkaline electrolytes to verify the applicability of the in-line CFRS method. Raman spectra were recorded under high current conditions, where one of the peaks used for calculating the peak ratio decreases significantly and may be obscured by the background. KOH electrolytes (0.1 and 1 M) were tested due to their relevance in alkaline water electrolysis,²⁸ while 1 M K_2CO_3 was used to emulate pH measurements relevant to CO_2 reduction in alkaline media.²⁹ Interfacial pH values at a

nominal distance of 10 μm from the electrode surface were calculated using the calibration curve in **Figure S3**, with results summarized in **Table S7**. SNR values were calculated as previously defined and are reported in **Table S8**.

Table S7. In-line CFRS measurement properties under different alkaline electrolytes.

Electrolyte (+ 0.5 PMP)	j (mA·cm 2)	Intensity @ 936 cm $^{-1}$	Intensity @ 990 cm $^{-1}$	Peak ratio	pH
0.1 M KOH	200	39.50	21.50	1.84 ± 0.06	12.71 ± 0.05
0.1 M KOH	-200	32.50	14.00	$*2.32 \pm 0.07$	$*13.13 \pm 0.06$
1 M KOH	200	31.20	11.00	$*2.84 \pm 0.09$	$*13.58 \pm 0.08$
1 M KOH	-200	28.80	9.50	$*3.03 \pm 0.10$	$*13.75 \pm 0.09$
1 M K ₂ CO ₃	200	21.30	32.40	0.66 ± 0.06	11.68 ± 0.05
1 M K ₂ CO ₃	-200	21.80	19.00	1.15 ± 0.05	12.11 ± 0.04

The uncertainty indicates the standard deviation derived from three replicate measurements.

*The intensities @ 990 cm $^{-1}$ are at the same level as the noise; thus, the pH is not reliable.

Table S8. Average SNR values from in-line CFRS measurements under different alkaline electrolytes.

Electrolyte (+ 0.5 PMP)	j (mA·cm 2)	Intensity @ 990 cm $^{-1}$	Intensity @ 936 cm $^{-1}$	Intensity @ 700 cm $^{-1}$	SNR (990/700)	SNR (936/700)
0.1 M KOH	200	21.50	39.50	11.86	2.80	8.02
0.1 M KOH	-200	14.00	32.50	10.56	$*1.06$	6.75
1 M KOH	200	11.00	31.20	9.97	$*0.32$	6.72
1 M KOH	-200	9.50	28.80	11.20	$*-0.51$	5.26
1 M K ₂ CO ₃	200	32.40	21.30	8.64	8.08	4.30
1 M K ₂ CO ₃	-200	19.00	21.80	7.54	4.17	5.19

Average SNR values derived from three replicate measurements.

*The SNR falls below the recommended threshold (SNR = 2–3).²⁷

The CFRS method is capable of estimating local pH under OER conditions for 0.1 M KOH (bulk pH = 13.23), as the PO₄³⁻/HPO₄²⁻ peak ratio (i.e., 1.84, **Table S7**) remains within the calibration range (**Figure S3**). However, the local pH becomes more alkaline under HER conditions, diminishing the HPO₄²⁻ peak intensity at 990 cm $^{-1}$ (i.e., 14.00, **Table S7**) near background noise levels (i.e., 10.56, **Table S8**). In 1 M KOH (bulk pH = 13.99), only the PO₄³⁻ signal is observed, and the HPO₄²⁻ peak is not discernible from the background. These

results indicate that the in-line CFRS method is not applicable in highly alkaline environments where only one species is detectable.

The CFRS method relies on the presence of acid and conjugate base forms (i.e., HPO_4^{2-} and PO_4^{3-}) to estimate local pH, as their ratio reflects the equilibrium composition at a given pH. When only one peak is visible, nearly all species exist in a single form, meaning changes in pH no longer produce a measurable shift in speciation. Based on the fractional composition of the $\text{PO}_4^{3-}/\text{HPO}_4^{2-}$ pair ($pK_{a,3} = 12.36$),¹² approximately 97.5% of the species exist as PO_4^{3-} at $\text{pH} = 13.36$ (i.e., one unit above $pK_{a,3}$). Therefore, the CFRS method using 0.5 M PMP can detect HPO_4^{2-} only when it constitutes more than ~2.5% of the PMP composition. Unless the local pH drops below ~13.3 during the experiment or the PMP concentration is increased above 0.5 M to increase the SNR, these small HPO_4^{2-} fractions will not be detectable. A detailed exploration of this aspect is beyond the scope of this study. However, researchers aiming to apply the CFRS method to other chemistries are encouraged to optimize the testing conditions to maximize the SNR.

In contrast, the carbonate-containing electrolyte (bulk pH = 11.87) exhibits clear PO_4^{3-} and HPO_4^{2-} peaks (**Figure S19**), allowing reliable pH quantification within the 11–13 pH range (**Table S7**) and SNR values above the recommended 2–3 threshold (**Table S8**).²⁷ A distinct peak appears at ~1068 cm⁻¹, which corresponds to the carbonate (CO_3^{2-}) ion.²⁹ It is important to note that, at around pH 12, only the CO_3^{2-} peak is detectable because more than 98% of carbonate species exist as CO_3^{2-} , consistent with the $\text{HCO}_3^-/\text{CO}_3^{2-}$ equilibrium ($pK_a = 10.3$).¹² Previous Raman-based approaches using the $\text{HCO}_3^-/\text{CO}_3^{2-}$ pair at higher concentrations (e.g., 3 M KHCO_3) also relied on the presence of both species and are therefore only applicable within a narrower pH window (~8 to ~11).²⁹

Our in-line CFRS method enables pH quantification in carbonate-containing systems at more alkaline pH (up to ~13.3) using relatively low PMP concentrations (0.5 M). Although increasing PMP concentration could enhance SNR and extend the measurable range, such adjustments may also affect other system properties and should be made with caution.

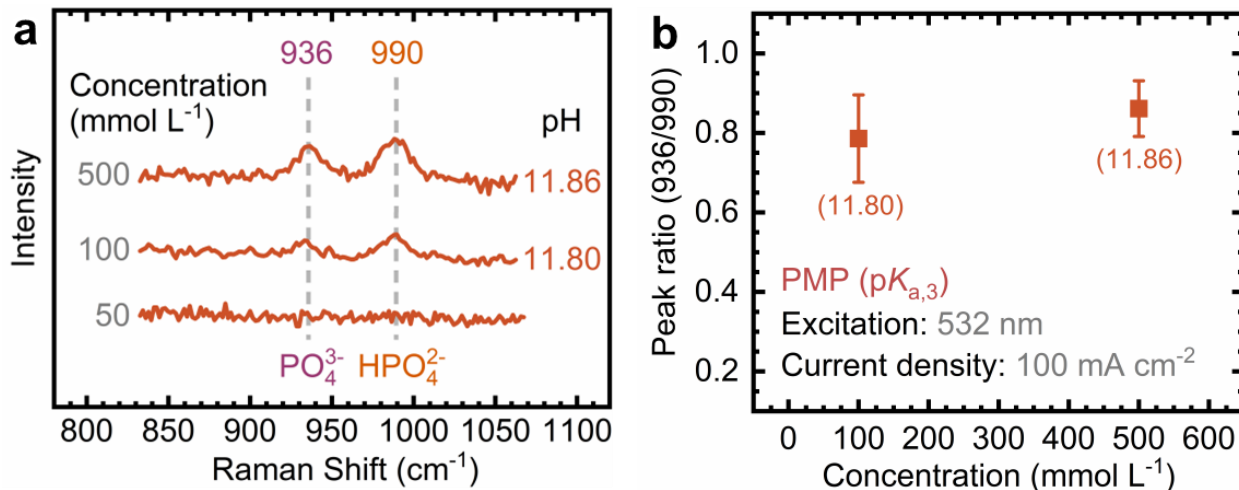


Figure S20. Effect of the PMP electrolyte concentration on the observed response during in-line CFRS experiments under alkaline conditions ($pK_{a,3} = 12.36$): (a) Raman spectra recorded at varying PMP electrolyte concentrations, and (b) plot of the phosphate/hydrogen phosphate peak ratio as a function of the concentration. The pH values in parentheses are estimated using the calibration curve shown in **Figure S3**. Data were collected with the laser beam located nominally 10 μm from the electrode surface. A current density of 100 $\text{mA}\cdot\text{cm}^{-2}$ was applied in all experiments. Flow rate: 100 $\text{mL}\cdot\text{min}^{-1}$.

Supporting note: The PMP electrolyte concentration was optimized to increase the SNR. Although 100 and 500 mM PMP yield similar pH values based on peak ratios (**Figure S20b**), the 100 mM PMP electrolyte exhibits lower peak intensities, particularly for the PO₄³⁻ peak, which could be misinterpreted as background noise. **Table S9** shows that increasing PMP concentration from 100 to 500 mM intensifies the signal by approximately 12 times, while 50 mM PMP does not exhibit significant PO₄³⁻/HPO₄²⁻ peaks. **Table S10** shows that 100 and 500 mM PMP peaks are above the recommended 2–3 SNR threshold.

Table S9. CFRS measurement properties under different PMP electrolyte concentrations.

Concentration (mmol·L ⁻¹)	Intensity @ 936 cm ⁻¹	Intensity @ 990 cm ⁻¹	Peak ratio	pH
50	12.00	17.36	*0.96 ± 0.08	*11.95 ± 0.07
100	31.91	40.61	0.79 ± 0.11	11.80 ± 0.10
500	63.50	73.75	0.86 ± 0.07	11.86 ± 0.06

The uncertainty indicates the standard deviation derived from three replicate measurements.

*The signal intensities are at the same level as the noise; thus, the pH is not considered reliable.

Table S10. SNR estimation from in-line CFRS measurements at different PMP electrolyte concentrations.

Concentration (mmol·L ⁻¹)	Intensity @ 990 cm ⁻¹	Intensity @ 936 cm ⁻¹	Intensity @ 700 cm ⁻¹	SNR (990/700) @ 100 mA·cm ⁻²	SNR (936/700) @ 100 mA·cm ⁻²
50	17.36	12.00	12.46	*1.39	*-0.13
100	40.61	31.91	15.09	6.57	4.33
500	73.75	63.50	10.67	19.31	16.17

*The SNR falls below the recommended threshold (SNR = 2–3).²⁷

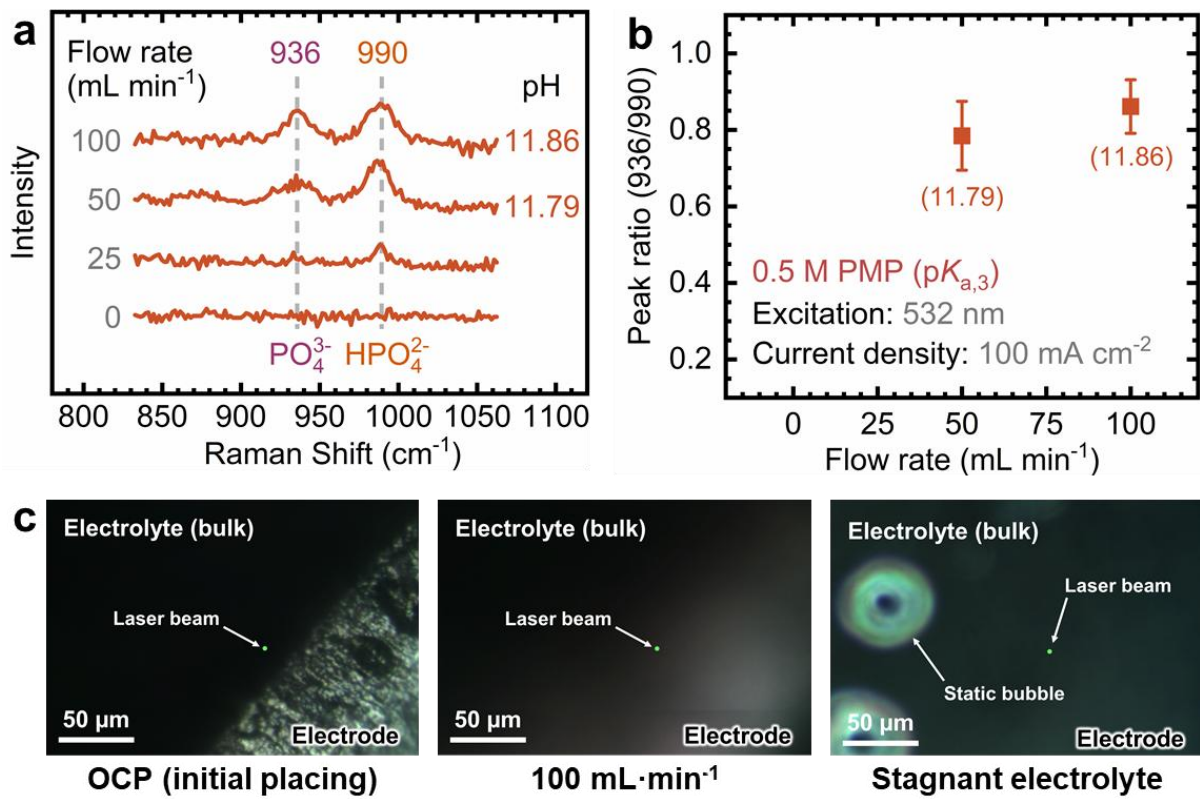


Figure S21. Effect of the flow rate on the observed response during in-line CFRS experiments under alkaline conditions (0.5 M PMP, $\text{pK}_{\text{a},3} = 12.36$): (a) Raman spectra recorded at varying flow rates, and (b) plot of the phosphate/hydrogen phosphate peak ratio as a function of the flow rate. The pH values in parentheses are estimated using the calibration curve shown in **Figure S3**. (c) Raman microscope images of the electrode-electrolyte interface under three flow conditions: laser placement at OCP (no current), real-time imaging at $100 \text{ mL}\cdot\text{min}^{-1}$, and bubble growth in a stagnant electrolyte. A current density of $100 \text{ mA}\cdot\text{cm}^{-2}$ was applied in all experiments at varying flow rates.

Supporting note: A flowing electrolyte is required to remove gas bubbles that interfere with the spectral acquisition and block the electrode surface. Bubble removal during in-line CFRS can be observed in this [video](#). **Table S11** shows that increasing the flow rate from 50 to $100 \text{ mL}\cdot\text{min}^{-1}$ enhances the signal approximately threefold, while a stagnant electrolyte prevents detection due to bubble interference. Even a $25 \text{ mL}\cdot\text{min}^{-1}$ flow rate cannot produce distinguishable Raman signals. **Table S12** shows that peaks for 50 and $100 \text{ mL}\cdot\text{min}^{-1}$ flow rates are above the recommended 2–3 SNR threshold, with the SNR nearly doubling at $100 \text{ mL}\cdot\text{min}^{-1}$. These results highlight the critical role of electrolyte flow in our in-line CFRS method and underscore the need for precise flow control.

Table S11. CFRS measurement properties under different electrolyte flow rates.

Flow rate (mL·min ⁻¹)	Intensity @ 936 cm ⁻¹	Intensity @ 990 cm ⁻¹	Peak ratio	pH
0	16.25	13.75	*1.18 ± 0.11	*12.14 ± 0.10
25	23.56	37.00	*0.58 ± 0.09	*11.62 ± 0.08
50	52.56	67.00	0.78 ± 0.09	11.79 ± 0.08
100	63.50	73.75	0.86 ± 0.07	11.86 ± 0.06

The uncertainty indicates the standard deviation derived from three replicate measurements.

*The signal intensities are at the same level as the noise; thus, the pH is not considered reliable.

Table S12. SNR estimation from in-line CFRS measurements at different flow rates.

Flow rate (mL·min ⁻¹)	Intensity @ 990 cm ⁻¹	Intensity @ 936 cm ⁻¹	Intensity @ 700 cm ⁻¹	SNR (990/700) @ 100 mA·cm ⁻²	SNR (936/700) @ 100 mA·cm ⁻²
0	13.75	16.25	14.57	*-0.21	*0.44
25	37.00	23.56	16.80	4.93	*1.16
50	67.00	52.56	16.78	12.26	8.73
100	73.75	63.50	10.67	19.31	16.17

*The SNR falls below the recommended threshold (SNR = 2–3).²⁷

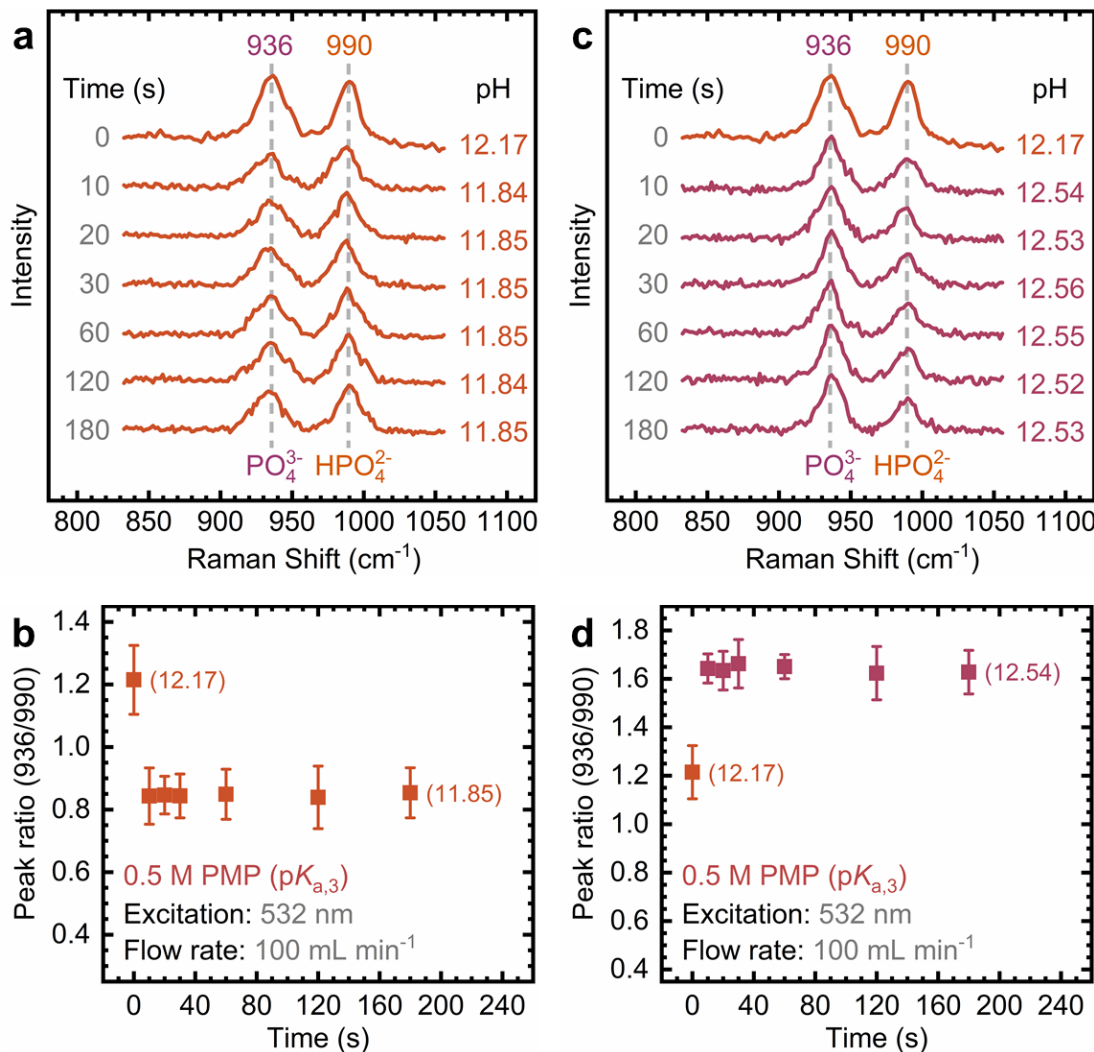


Figure S22. Effect of the spectra collection at different intervals during in-line CFRS experiments under alkaline conditions ($\text{pK}_{\text{a},3} = 12.36$): (a) Raman spectra recorded at different times during a chronopotentiometry (CP) step at $100 \text{ mA}\cdot\text{cm}^{-2}$ and (b) plot of the phosphate/hydrogen phosphate peak ratios as a function of the time. (c) Raman spectra recorded at different times during a CP step at $-100 \text{ mA}\cdot\text{cm}^{-2}$ and (d) plot of the phosphate/hydrogen phosphate peak ratios as a function of time. CP runs lasted 180 s, with each Raman spectrum collected in a single accumulation using a 10-second acquisition time (for this particular experiment). The pH values are estimated using the calibration curve shown in **Figure S3**. Data were collected with the laser beam located nominally $10 \mu\text{m}$ from the electrode surface.

Supporting note: The experiment in **Figure S22** was conducted to assess the validity of averaging three scans over 180 seconds. From the first spectrum, the pH drops sharply and remains virtually unchanged throughout the CP step. This behavior is consistent with the rapid pH drop (1–2 seconds) reported by the Surendranath group.³⁰

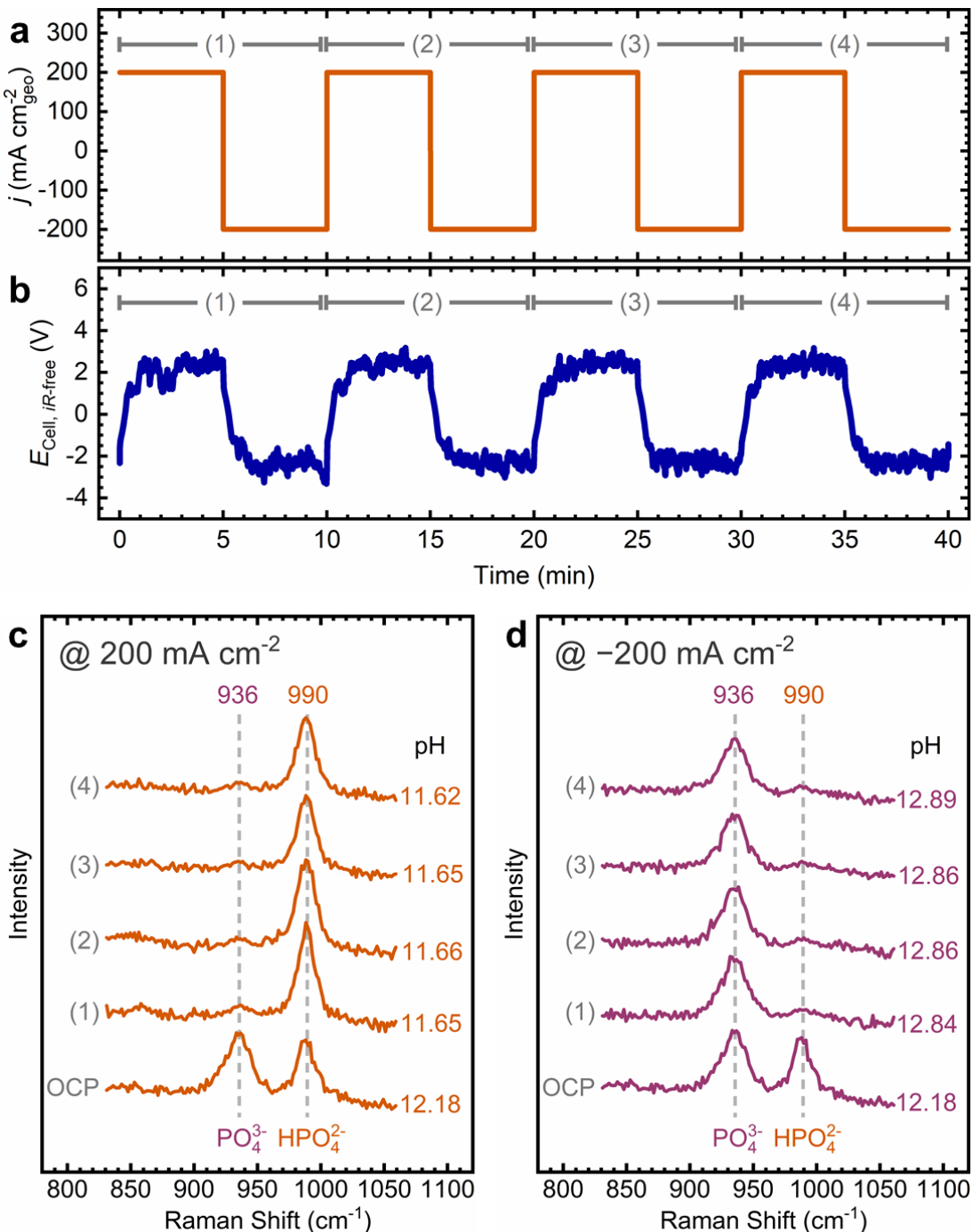


Figure S23. Effect of variable operation during in-line CFRS experiments under alkaline conditions ($\text{p}K_{\text{a},3} = 12.36$): (a) Current densities and (b) corresponding iR -corrected cell potential during the alternating current experiment. (c) Raman spectra recorded during OER steps at $200 \text{ mA}\cdot\text{cm}^{-2}$ and (d) HER steps at $-200 \text{ mA}\cdot\text{cm}^{-2}$. Galvanostatic steps lasted 300 seconds, with each Raman spectrum collected in five accumulations using a 60-second acquisition time (for this particular experiment). The pH values are estimated using the calibration curve shown in **Figure S3**. Data were collected with the laser beam located nominally $10 \mu\text{m}$ from the electrode surface. Flow rate: $100 \text{ mL}\cdot\text{min}^{-1}$.

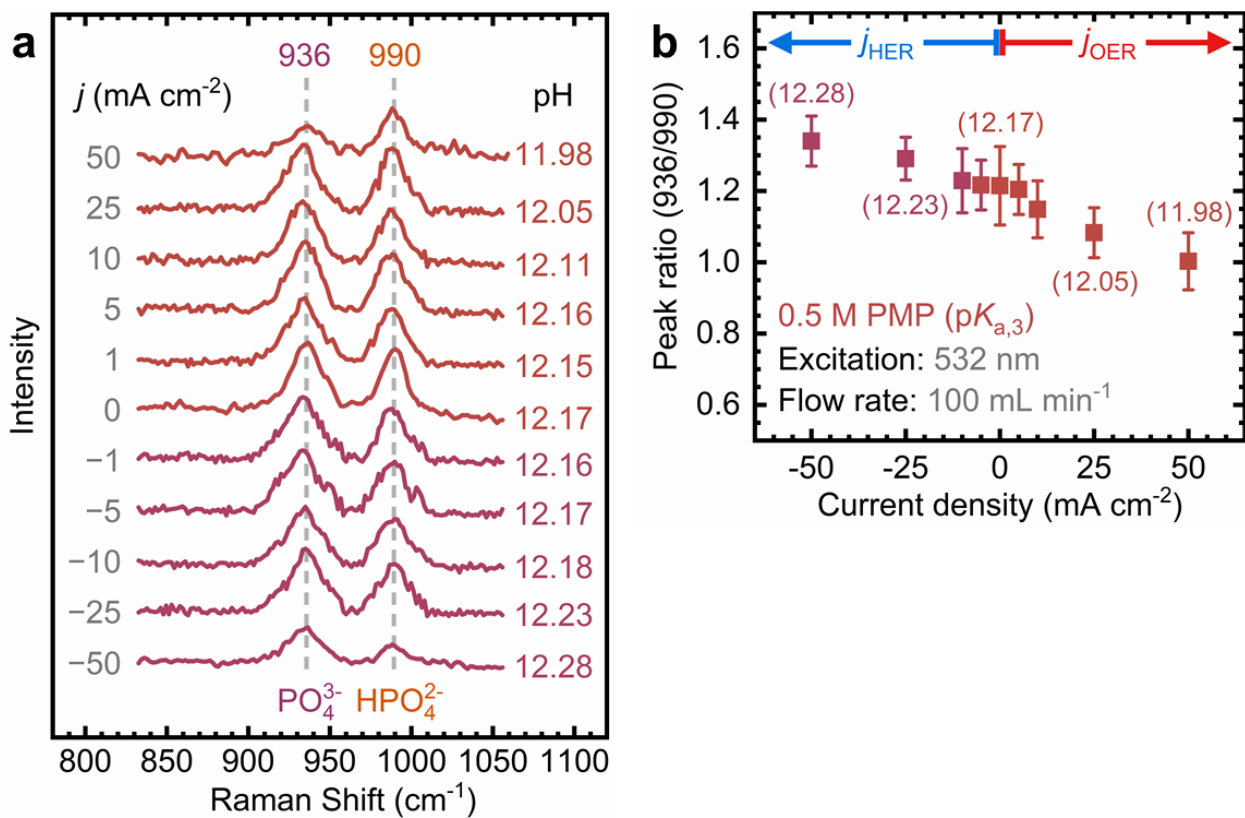


Figure S24. Effect of low current densities on local pH estimated from in-line CFRS experiments under alkaline conditions ($\text{pK}_{\text{a},3} = 12.36$): (a) Raman spectra recorded at varying current densities, and (b) plot of the phosphate/hydrogen phosphate peak ratio as a function of current density. The pH values are estimated using the calibration curve shown in **Figure S3**. Data were collected with the laser beam located nominally $10 \mu\text{m}$ from the electrode surface. Flow rate: $100 \text{ mL}\cdot\text{min}^{-1}$.

Supporting note: The applied current density was optimized to identify the threshold at which a significant shift in the phosphate/hydrogen phosphate peak ratio occurs. From **Figure S24b**, noticeable peak intensity changes emerge at $\pm 25 \text{ mA}\cdot\text{cm}^{-2}$, but only at $\pm 50 \text{ mA}\cdot\text{cm}^{-2}$, the deviation from OCP becomes statistically significant ($p < 0.05$), particularly for the OER. These results confirm that the in-line CFRS method can detect local pH fluctuations reliably at currents beyond $\pm 50 \text{ mA}\cdot\text{cm}^{-2}$.

These experiments indicate that the in-line CFRS method is highly responsive to operating conditions. Researchers using the method are encouraged to optimize experimental parameters (e.g., PMP electrolyte concentration, flow rate) to enhance sensitivity at lower currents.

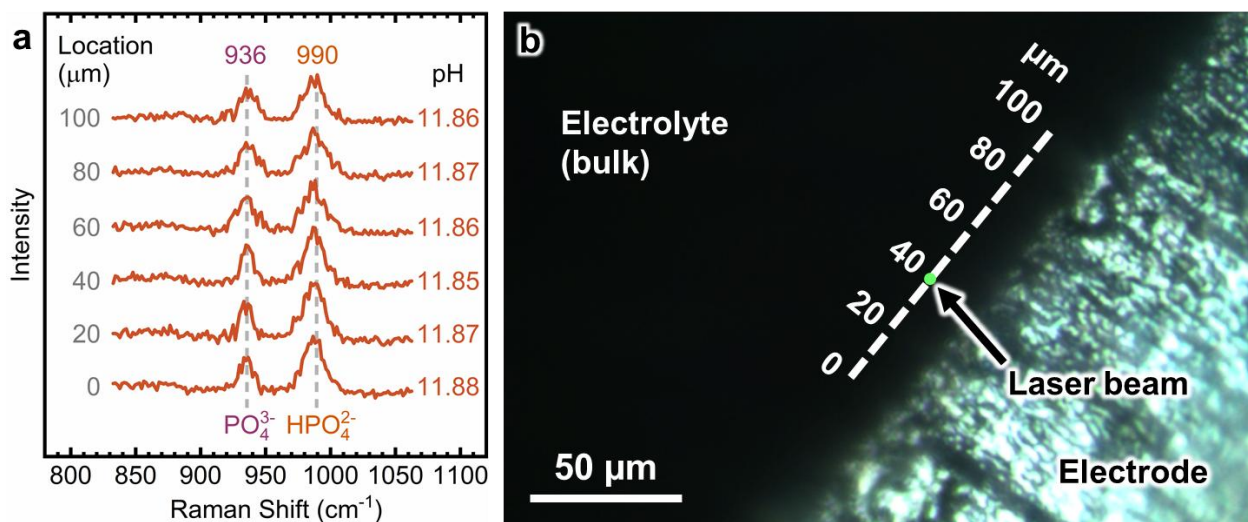


Figure S25. Effect of the lateral laser beam position during in-line CFRS experiments under alkaline conditions ($\text{pK}_{\text{a},3} = 12.36$): (a) Raman spectra recorded at varying positions parallel to the electrode surface, all nominally 10 μm from the electrode. pH values are estimated using the calibration curve in **Figure S3**. (b) Raman microscope image of the electrode-electrolyte interface, indicating the lateral positions where spectra were collected. Additional experimental conditions: excitation wavelength: 532 nm, current density: 100 $\text{mA}\cdot\text{cm}^{-2}$, flow rate: 100 $\text{mL}\cdot\text{min}^{-1}$.

Supporting note: The Raman spectra and corresponding local pH values from the calibration curve remain consistent as the laser beam scans parallel to the electrode surface. However, this measurement is limited to a region of 100 μm , where the electrode surface is relatively flat, and micron-scale roughness might not significantly influence pH gradients. This behavior may not hold in other areas, such as near the electrode edge, where surface irregularities are more pronounced, or at the flow cell inlet, where hydrodynamics likely deviate from those in the center of the flow channel. While our flow cell was not designed to examine inlet effects or electrode morphology, future studies could explore these aspects in greater detail.

References

- (1) Lu, S.; Zhang, Z.; Zhang, B.; Shi, Y. Insight into the Change in Local pH near the Electrode Surface Using Phosphate Species as the Probe. *J. Phys. Chem. Lett.* **2023**, *14* (46), 10457–10462. <https://doi.org/10.1021/acs.jpclett.3c02919>.
- (2) Lackey, H. E.; Nelson, G. L.; Lines, A. M.; Bryan, S. A. Reimagining pH Measurement: Utilizing Raman Spectroscopy for Enhanced Accuracy in Phosphoric Acid Systems. *Anal. Chem.* **2020**, *92* (8), 5882–5889. <https://doi.org/10.1021/acs.analchem.9b05708>.
- (3) Kucernak, A. R.; Wang, H.; Lin, X. Avoid Using Phosphate Buffered Saline (PBS) as an Electrolyte for Accurate OER Studies. *ACS Energy Lett.* **2024**, *9* (8), 3939–3946. <https://doi.org/10.1021/acsenergylett.4c01589>.
- (4) Márquez-Montes, R. A.; Collins-Martínez, V. H.; Pérez-Reyes, I.; Chávez-Flores, D.; Graeve, O. A.; Ramos-Sánchez, V. H. Electrochemical Engineering Assessment of a Novel 3D-Printed Filter-Press Electrochemical Reactor for Multipurpose Laboratory Applications. *ACS Sustain. Chem. Eng.* **2020**, *8* (9), 3896–3905. <https://doi.org/10.1021/acssuschemeng.9b07368>.
- (5) Szántó, D. A.; Cleghorn, S.; Ponce-de-León, C.; Walsh, F. C. The Limiting Current for Reduction of Ferricyanide Ion at Nickel: The Importance of Experimental Conditions. *AIChE J.* **2008**, *54* (3), 802–810. <https://doi.org/10.1002/aic.11420>.
- (6) Recio, F. J.; Herrasti, P.; Vazquez, L.; Ponce de León, C.; Walsh, F. C. Mass Transfer to a Nanostructured Nickel Electrodeposit of High Surface Area in a Rectangular Flow Channel. *Electrochim. Acta* **2013**, *90*, 507–513. <https://doi.org/10.1016/j.electacta.2012.11.135>.
- (7) Griffiths, M.; de León, C. P.; Walsh, F. C. Mass Transport in the Rectangular Channel of a Filter-Press Electrolyzer (the FM01-LC Reactor). *AIChE J.* **2005**, *51* (2), 682–687. <https://doi.org/10.1002/aic.10311>.
- (8) Cañizares, P.; García-Gómez, J.; Fernández de Marcos, I.; Rodrigo, M. A.; Lobato, J. Measurement of Mass-Transfer Coefficients by an Electrochemical Technique. *J. Chem. Educ.* **2006**, *83* (8), 1204. <https://doi.org/10.1021/ed083p1204>.
- (9) Bard, A. J.; Faulkner, L. R.; White, H. S. *Electrochemical Methods: Fundamentals and Applications*, Third.; John Wiley & Sons: New York, 2022.
- (10) Zheng, W. Beginner's Guide to Raman Spectroelectrochemistry for Electrocatalysis Study. *Chemistry—Methods* **2022**, *3*, e202200042. <https://doi.org/10.1002/cmtd.202200042>.
- (11) Veroneau, S. S.; Hartnett, A. C.; Ryu, J.; Hong, H.; Costentin, C.; Nocera, D. G. A Straightforward Model for Quantifying Local pH Gradients Governing the Oxygen Evolution Reaction. *J. Am. Chem. Soc.* **2024**, *146* (42), 28925–28931. <https://doi.org/10.1021/jacs.4c09521>.

- (12) Harris, D. C.; Lucy, C. A. *Quantitative Chemical Analysis*, Ninth Edition.; W. H. Freeman and Company, 2016.
- (13) Resasco, J.; Lum, Y.; Clark, E.; Zeledon, J. Z.; Bell, A. T. Effects of Anion Identity and Concentration on Electrochemical Reduction of CO₂. *ChemElectroChem* **2018**, 5 (7), 1064–1072. <https://doi.org/10.1002/celc.201701316>.
- (14) Gupta, N.; Gattrell, M.; MacDougall, B. Calculation for the Cathode Surface Concentrations in the Electrochemical Reduction of CO₂ in KHCO₃ Solutions. *J Appl Electrochem* **2006**, 36 (2), 161–172. <https://doi.org/10.1007/s10800-005-9058-y>.
- (15) Rumble, J. R.; Brunno, T. J.; Doa, M. J. *CRC Handbook of Chemistry and Physics 105th Edition*; CRC Press/Taylor and Francis Group: Boca Raton, 2024.
- (16) Lucy, C. A. Is Your Henderson–Hasselbalch Calculation of Buffer pH Correct? *J. Chem. Educ.* **2023**, 100 (6), 2418–2422. <https://doi.org/10.1021/acs.jchemed.2c01203>.
- (17) Green, L. W.; Kruus, P.; McGuire, M. J. Acid Dissociation Constants and Rates as Studied by Ultrasonic Absorption. *Can. J. Chem.* **1976**, 54 (20), 3152–3162. <https://doi.org/10.1139/v76-449>.
- (18) Jiang, P.-Y.; Katsumura, Y.; Domae, M.; Ishikawa, K.; Nagaishi, R.; Ishigure, K.; Yoshida, Y. Pulse Radiolysis Study of Concentrated Phosphoric Acid Solutions. *J. Chem. Soc., Faraday Trans.* **1992**, 88 (22), 3319–3322. <https://doi.org/10.1039/FT9928803319>.
- (19) Buxton, G. V.; Greenstock, C. L.; Helman, W. P.; Ross, A. B. Critical Review of Rate Constants for Reactions of Hydrated Electrons, Hydrogen Atoms and Hydroxyl Radicals ($\cdot\text{OH}/\cdot\text{O}^-$) in Aqueous Solution. *J. Phys. Chem. Ref. Data* **1988**, 17 (2), 513–886. <https://doi.org/10.1063/1.555805>.
- (20) Maruthamuthu, P.; Neta, P. Phosphate Radicals. Spectra, Acid-Base Equilibria, and Reactions with Inorganic Compounds. *J. Phys. Chem.* **1978**, 82 (6), 710–713. <https://doi.org/10.1021/j100495a019>.
- (21) Singh, M. R.; Goodpaster, J. D.; Weber, A. Z.; Head-Gordon, M.; Bell, A. T. Mechanistic Insights into Electrochemical Reduction of CO₂ over Ag Using Density Functional Theory and Transport Models. *Proceedings of the National Academy of Sciences* **2017**, 114 (42), E8812–E8821. <https://doi.org/10.1073/pnas.1713164114>.
- (22) Bohra, D.; Chaudhry, J. H.; Burdyny, T.; Pidko, E. A.; Smith, W. A. Modeling the Electrical Double Layer to Understand the Reaction Environment in a CO₂ Electrocatalytic System. *Energy Environ. Sci.* **2019**, 12 (11), 3380–3389. <https://doi.org/10.1039/C9EE02485A>.
- (23) Bernt, M.; Gasteiger, H. A. Influence of Ionomer Content in IrO₂/TiO₂ Electrodes on PEM Water Electrolyzer Performance. *J. Electrochem. Soc.* **2016**, 163 (11), F3179. <https://doi.org/10.1149/2.0231611jes>.

- (24) Bernt, M.; Siebel, A.; Gasteiger, H. A. Analysis of Voltage Losses in PEM Water Electrolyzers with Low Platinum Group Metal Loadings. *J. Electrochem. Soc.* **2018**, 165 (5), F305–F314. <https://doi.org/10.1149/2.0641805jes>.
- (25) How to Calculate Signal to Noise Ratio. <https://www.horiba.com/usa/scientific/technologies/fluorescence-spectroscopy/how-to-calculate-signal-to-noise-ratio/> (accessed 2025-03-12).
- (26) Miller, J.; Miller, J.; Miller, R. *Statistics and Chemometrics for Analytical Chemistry*, Seventh Edition.; Pearson Education: Harlow, England, 2018.
- (27) Skoog, D. A.; Holler, F. J.; Crouch, S. R. *Principles of Instrumental Analysis*, 7th ed.; Cengage Learning, 2017.
- (28) Márquez, R. A.; Kawashima, K.; Son, Y. J.; Castelino, G.; Miller, N.; Smith, L. A.; Chukwuneke, C. E.; Mullins, C. B. Getting the Basics Right: Preparing Alkaline Electrolytes for Electrochemical Applications. *ACS Energy Lett.* **2023**, 8 (2), 1141–1146. <https://doi.org/10.1021/acsenergylett.2c02847>.
- (29) Zhang, Z.; Melo, L.; Jansonius, R. P.; Habibzadeh, F.; Grant, E. R.; Berlinguette, C. P. pH Matters When Reducing CO₂ in an Electrochemical Flow Cell. *ACS Energy Lett.* **2020**, 5 (10), 3101–3107. <https://doi.org/10.1021/acsenergylett.0c01606>.
- (30) Sauvé, E. R.; Tang, B. Y.; Razdan, N. K.; Toh, W. L.; Weng, S.; Surendranath, Y. Open Circuit Potential Decay Transients Quantify Interfacial pH Swings during High Current Density Hydrogen Electrocatalysis. *Joule* **2024**, 8 (3), 728–745. <https://doi.org/10.1016/j.joule.2024.01.004>.